ORIGINAL PAPER-EXPLORATION GEOLOGY

Formation mechanical mechanism of low-angle fractures in pre-salt carbonate reservoirs: a case study from Carboniferous KT-I formation of the NT oilfield in the eastern margin of the Precaspian Basin, Kazakhstan

Changhai Li[1,2] · Lun Zhao[2] · Bo Liu[3] · Weiqiang Li[4] · Kaibo Shi[3] · Wenqi Zhao[2] · Jianxin Li[2] · Qiang Zhu[1] · Yunhai Li[1] · Caiqin Ma[1]

Abstract

Fracture is an important factor that affects the oil and gas productivity of carbonate reservoirs. Much researches have been done on the origin of high-angle fractures in carbonate reservoirs, but few efforts have been made on the genetic mechanical mechanism of low-angle fractures. Based on the seismic data, core data, conventional logging data and rock mechanics experimental data, combined with three-dimensional in situ stress field simulation methods, the features, formation geological conditions and genetic mechanical mechanism of low-angle fractures (LAFs) were analyzed by applying Coulomb–Moore criterion, Griffith criterion and non-coordination criterion. The proportion of the number of shear fractures is as high as 90.2%, while that of tensile fractures is only 9.8% in the study area. Shear fractures are mainly unfilled fractures, and tensile fractures are mainly partially filled fractures. The LAFs were formed in the second tectonic movement, in which the knee-fold structure with high in the west and low in the east developed in the study area. The buried depth of most parts of the KT-I formation is 800 m when the study area develops the knee-fold structure, with a maximum depth of 1800 m and a minimum buried depth of 70 m, and the dip angle of the steepest part of the stratum is about 20°. A large number of LAFs were formed in the study area under the joint influence of tectonics and abnormally high pressure of water, including near-horizontal LAFs in the non-weak fabrics section (type I low-angle shear fractures), the LAFs having a certain angle with bedding in the non-weak fabrics section (type II low-angle shear fractures) and near-horizontal LAFs in the weak fabrics section (type III low-angle shear fractures). The formation of type I and type II low-angle shear fractures follows the Coulomb–Moore criterion. Type I low-angle shear fractures are formed in strata with a certain dip angle, while type II low-angle shear fractures are formed in near-horizontal strata. Type III low-angle shear fractures are formed under the comprehensive influence of pre-existing weak fabrics and strong horizontal extrusion, which follows the non-coordination criterion. Low-angle tensile fractures are mainly caused by abnormally high pressure and reverse faults in the study area, following Griffith's criterion. The research in this paper not only reveals the formation mechanical mechanism of LAFs in pre-salt carbonate reservoirs but also provides guidance for the prediction of LAFs and solving the problem of water channeling caused by LAFs in oil fields.

Keywords Pre-salt carbonate reservoir · Low-angle fractures · In situ stress field simulation · Formation mechanism · NT oilfield · Precaspian Basin

✉ Changhai Li
chhli.sipc@sinopec.com

✉ Weiqiang Li
liwq_hz@petrochina.com.cn

1 Sinopec International Petroleum Exploration and Production Corporation, No.6 Huixin East Street, Chaoyang, Beijing 100029, China

2 PetroChina Research Institute of Petroleum Exploration and Development, Beijing 100083, China

3 School of Earth and Space Sciences, Peking University, Beijing 100871, China

4 PetroChina Hangzhou Research Institute of Geology, No.920 XiXi Road, Xihu District, Hangzhou 310023, Zhejiang Province, China

🌀 Springer

Abbreviations

LAFs	Low-angle fractures
Type I low-angle shear fractures	Near-horizontal LAFs in the non-weak fabrics section
Type II low-angle shear fractures	The low-angle fractures having a certain angle with bedding in the non-weak fabrics section
Type III low-angle shear fractures	Near-horizontal low-angle fractures in the weak fabrics section
3D	Three-dimensional

List of symbols

C	The shear strength of the rock
C_b	Coefficient of formation volume compressibility (GPa^{-1})
C_{ma}	Skeleton volume compression coefficient (GPa^{-1})
C_W	Shear strength (MPa)
C_0	Rock shear strength (GPa)
E	Dynamic Young's modulus (GPa)
f_{aw}	Fracture coefficient of the pre-existing weak fabrics (MPa)
f_{aF}	The activity coefficient of the pre-existing fault (MPa)
G	Shear modulus (GPa)
g	The acceleration of gravity (m/s^2)
H	The buried depth of the target layer (m)
K	Bulk modulus (GPa)
n	The total number of the numerical value smaller than z_1
Pp	The hydrostatic pressure (MPa)
S_C	Uniaxial compressive strength (GPa)
S_T	Tensile strength of rock (GPa)
$\tan \varphi$	The coefficient of internal friction in the rock
Δt_s	S-wave sonic interval transit time (us/m)
Δt_p	P-wave sonic interval transit time (us/m)
Δt_{ms}	Rock skeleton S-wave sonic interval transit time (us/m)
Δt_{mp}	Rock skeleton P-wave sonic interval transit time (us/m)
v_s, v_{mas}	Formation S-wave velocity and rock skeleton S-wave velocity (m/s)
v_p, v_{map}	Formation P-wave velocity and rock skeleton P-wave velocity (m/s)
V_p	The shear wave velocity (m/s)
V_{sh}	Clay content
Z_1	The variables smaller than z_1
z_1, z_2 and z_N	Any numerical value in the set of data
Z_2	The variables smaller than z_2
Z_n	The variables smaller than z_n
α	The angle between the intersection of the weak fabrics on the σ_2–σ_3 plane and the minimum principal stress σ_3
β	The internal friction angle
θ	The angle between the weak fabrics and the direction of σ_1
μ	Dynamic Poisson's modulus
μ_w	The internal friction coefficient
ρ	Rock density (kg/m^3)
ρ_b, ρ_{ma}	Formation bulk density and rock skeleton bulk density (g/cm^3)
σ	Normal stress
σ_H	Horizontal maximum principal stress (MPa)
σ_h	Horizontal minimum principal stress (MPa)
σ_T	The critical rupture pressure (MPa)
σ_v	The vertical stress (MPa)
σ_1	The first principal stress (MPa)
σ_2	The second principal stress (MPa)
σ_3	The third principal stress (MPa)
τ	Shear stress

$[\tau_n]$	The shear stress corresponding to the same normal stress on the rupture line (MPa)
τ_n	Shear stress for the rock with pre-existing weak fabrics (MPa)
Φ	Porosity (%)
φ	Rock internal friction angle (°)

Introduction

Carbonate is an important oil and gas reservoir, which accounts for about 40% of geological reserves and 60% of crude oil production in the world (Bagrintseva 2015). Almost all carbonate reservoirs are related to fractures, such as Kashagan Oilfield in Central Asia (Kabiyev et al. 2012), X Oilfield in the Middle East (Sima et al. 2014) and pre-salt carbonate oilfield in Brazil (Huang et al. 2022). Fracture is an important factor affecting the production of carbonate reservoirs, for example, the productivity of a single well in the Shunbei Oilfield is mainly related to the distribution and intensity of fractures (Ma et al. 2022). Therefore, it is of great significance to study fractures in carbonate reservoirs. The previous studies on fractures mainly focused on high-angle fractures and conducted in-depth research on the identification, classification, origins, characterization and prediction of high-angle fractures (Nelson 2001). However, the research on low-angle fractures (LAFs) with a dip angle of less than 30° was mainly limited to the genetic model. According to the origin of low-angle fractures, the previous workers put forward three models: the LAFs induced by fault activity, the LAFs associated with fold formation and the LAFs formed due to overpressure (Séjourné et al. 2005). Both fault activity and fold formation lead to rock deformation and interlayer sliding of strata, which further induces the formation of low-angle fractures. Overpressure is mainly caused by the hydrocarbon generation of organic matter, and it results in formation pressure exceeding the strength of rock rupture, which causes the formation of low-angle fractures. The above-mentioned genetic models can well explain the origin of low-angle fractures. For example, Du et al. (2016) studied the genetic mechanism of LAFs in carbonate reservoirs of the Khorat Basin, Thailand, and pointed out that the LAFs along the pre-existing weak fabrics in the carbonate are caused by the impact of thrust faults. Although the previous workers have done a lot of solid work on the genetic model of low-angle fractures, there are relatively few studies on the mechanical genetic mechanism of low-angle fractures. Only Smart et al.

(2009, 2010) analyzed the mechanical genetic mechanism of LAFs caused by fault propagation folds under the extension background in the Sierra del Carmen in the Big Bend region of West Texas, USA. However, the research on the mechanical genetic mechanism of LAFs in pre-salt carbonate reservoirs caused by fault propagation folds under the compression background was seldom studied.

The NT oilfield is located on the eastern edge of the Precaspian Basin, and it is one of the largest oil and gas fields in the Precaspian Basin. Both high-angle fractures and LAFs have developed in this oilfield, and the complex fracture network leads to serious water channeling in the oilfield. The previous understanding of high-angle fractures in this oilfield is in-depth, but the research on LAFs in this oilfield is limited to its formation period, controlling factors and genetic model (Li et al. 2021). Hence, there is still a lack of research on the mechanical genetic mechanism of LAFs in this oilfield. The NT oilfield developed the LAFs caused by the fault propagation folds under the compression background (Li et al. 2021), which provides the chance to study the mechanical genetic mechanism of LAFs caused by fault propagation folds under the compression background. Based on the seismic data, core data, logging data and rock mechanics experimental data, this paper analyzes the types and characteristics of LAFs in the NT oilfield, and then restores the paleostruture during the formation of the LAFs with the guidance of fracture formation timing, and finally simulates the three-dimensional (3D) paleo-stress field during the formation of LAFs to reveal the mechanical mechanism of low-angle fractures.

Geological setting

The Precaspian Basin is one of the most important oil-bearing basins in the world, with a total area of 5×10^5 km^2 and a maximum sediment thickness of 12 km (Hu et al. 2014). The proven reserves of oil and gas are as high as 30×10^8 t in this basin (Miao et al. 2013). Many well-known large oil and gas fields, such as Astrakhan, Tenghiz and Kashagan, have been discovered. The Precaspian Basin is located in the northern part of the Caspian Sea, spanning Kazakhstan and Russia, and about 75% of the basin area is located in Kazakhstan. The Precaspian Basin can be further divided into four secondary structural blocks, including the northern step-fault belt, the central depression belt, the Astrakhan–Aktobins uplifted belt and the southeast depression belt (Fig. 1a and b). The basement of the basin is Archean and Proterozoic epimetamorphic rocks and gneiss, and all strata of Paleozoic, Mesozoic and Cenozoic are deposited (Fig. 2). The Permian Kungurian salt strata vertically divide the basin into three sets of strata, including the pre-salt strata, the
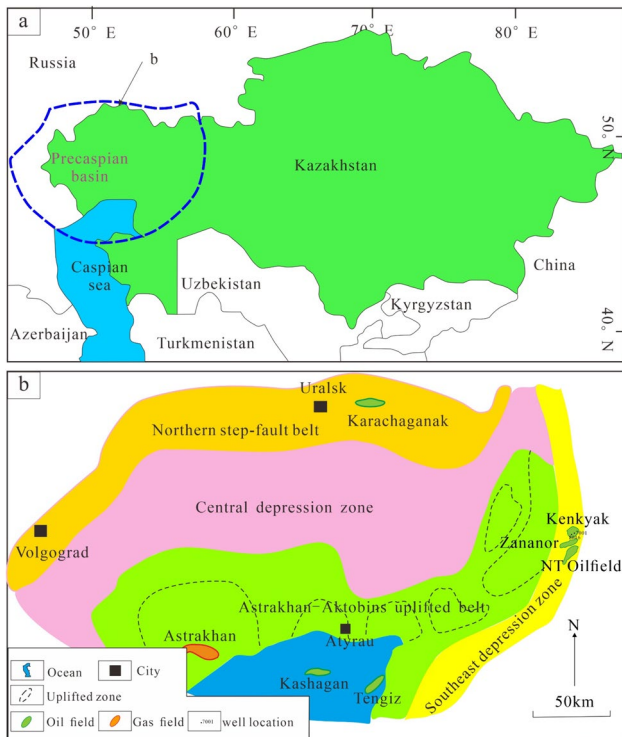
Fig. 1 Location and tectonic units of Precaspian Basin. **a** Location of the study area and **b** tectonic units of Precaspian Basin

salt-bearing strata and the sub-salt strata (Brunet et al. 1999). The NT oilfield is located in the central block of the eastern slope of the Zarkames–Yanbeks paleo-uplift in the southeast depression belt, and the target layer of this study is the pre-salt Carboniferous KT-I formation. The KT-I formation is divided into 10 sublayers from top to bottom, including A1, A2, A3, Б1, Б2, B1, B2, B3, B4 and B5, among which A1, A2 and A3 are deposited by evaporate platform facies, and the reservoirs consisted of dolomite and limestone. Layer A1 is almost completely missing due to the influence of stratum uplift and denudation. Layers Б1, Б2, B1 and B2 develop platform facies deposits, and the reservoirs are mainly limestone. Layers B2, B3, B4 and B5 deposit open platform facies, and the reservoirs are also mainly consist of limestone. The NT oilfield mainly experienced three stages of tectonic movements after sedimentation, including the structural compression movement in the early Permian forming the structural pattern of high in the west and low in the east of the study area; the Hercynian tectonic movement in the late Early Permian intensifying the structural pattern of high in the west and low in the east and the late Permian tectonic movement causing the structural inversion and forming a structural framework with high in the east

and low in the west. All three stages of tectonic movements are dominated by NW–SE tectonic compression. Due to the influence of the multi-stage tectonic movements, a large number of LAFs developed in the study area, accounting for 65% of the total number of fractures.

Methods and theory

Observation and statistics of core fracture parameters

By observing the 448.32-m core in the study area, the mechanical properties of LAFs with dip angles less than or equal to 30° in the study area were analyzed. Furthermore, according to the dip angle of LAFs and the relationship between the dip angle of fractures and the beddings, the types and characteristics of LAFs were identified. Besides, the filling characteristics of LAFs were counted based on the difference in fracture filling degree.

Restoration of paleostructure of the KT-I formation during the formation of low-angle fractures

The 3D paleostructure during the formation of the LAFs was restored to disclose the mechanical mechanics of low-angle fractures. Li et al. (2021) have verified that the formation period of low-angle fractures is in the second tectonic movement, thus the 3D paleostructure in the second tectonic movement of the KT-I formation was restored. The key steps in 3D paleostructure restoration include denudation recovery, fault removal, fold removal, compaction correction and paleowater depth correction (Jiu et al. 2012). In this study, the 3D paleostructure pattern was restored based on the automatic layer tracing technology and the paleostructure restoration technology in the Petrel software.

The deposition of the KT-I formation ended in the late Carboniferous. The study area developed the paleostructure of high in the west and low in the east in the early lower Permian due to the influence of the first tectonic movements. And later the study area deposited the sandstone strata in the lower Permian and the Kungurian salt strata in the upper Permian in order. The second tectonic movement developed during the beginning of the deposition of the Kungurian salt stratum. Therefore, if we want to restore the paleostructure of the KT-I formation during the second tectonic movement, it is necessary to flatten the top structure of the Kungurian salt stratum. However, due to the influence of the later tectonic movement, the salt stratum is severely deformed, which leads it difficult to restore the paleostructure during
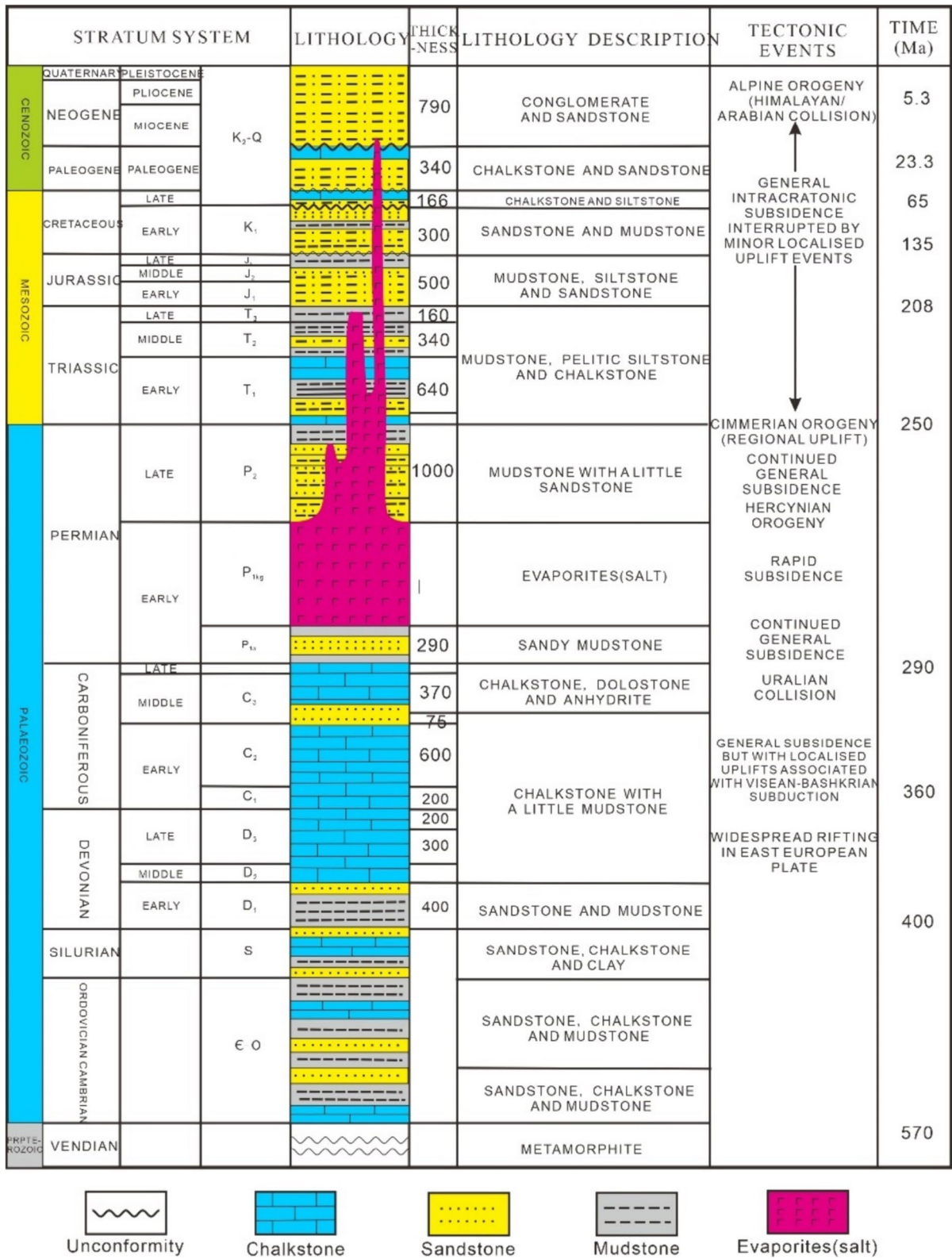
Fig. 2 Stratigraphic, lithological systems and tectonic events in the study area (Li et al. 2021)

the formation of the low-angle fractures. According to the previous structural evolution analysis results of the study area, it can be concluded that the salt stratum is uniformly deposited on the sandstone stratum; hence, the originally deposited salt stratum is regarded as a uniform thickness stratum (Jing et al. 2021). According to the previous studies, there is no denudation on the top of the Upper Permian stratum when LAFs are formed, thus it is unnecessary to restore denudation. The restoration of the paleostructure during the formation of the LAFs needs to remove the influence of fold and fault. The study area belongs to the internal deposition of the platform, and the study area is relatively small, thus the influence of compaction correction and paleowater depth correction can be ignored. To sum up, the study area only needs to remove the influence of fold and fault to restore the paleostructure during the formation of the low-angle fractures.

Based on the 3D seismic data in NT oilfield, different stratigraphic boundaries in the study area were identified, and the bottom surface of the Kungurian salt stratum was flattened, by which the 3D paleostructure during the formation of the LAFs was restored (Fig. 3). Specifically, several typical 2D seismic sections were manually identified in 3D seismic data, and based on the automatic layer tracing technology in the Petrel software, the present 3D structural map of the Permian top surface and the present 3D structural map of KT-I formation top surface were identified (Fig. 4a and b). By flattening the Permian top structural surface, the top structural surface of KT-I formation during the formation of the LAFs is restored. The 3D paleostructure is characterized by high in the west and low in the east during the formation of the low-angle fractures, which is consistent with the results of two-dimensional structural analysis results (Fig. 4c). The burial depth of the main part of the KT-I formation is 800 m, and the maximum burial depth can reach 1800 m, and the minimum burial depth is only 70 m. The dip angle of the steepest part of the stratum is about 20°. This phenomenon is a common occurrence of strata in the field, which conforms to the geological law, indicating that the restoration result of the paleostructure is reliable. Besides, based on the understanding of the fracture formation period and the previous research results on the evolution of organic matter in the study area (Tian et al. 2015; Zhu et al. 2018), it can be concluded that the buried depth of LAFs is less than 933.33 m, demonstrating that the organic matter is still in the immature stage. Therefore, the influence of hydrocarbon-generation pressurization on the formation of LAFs can be ruled out in the study area.
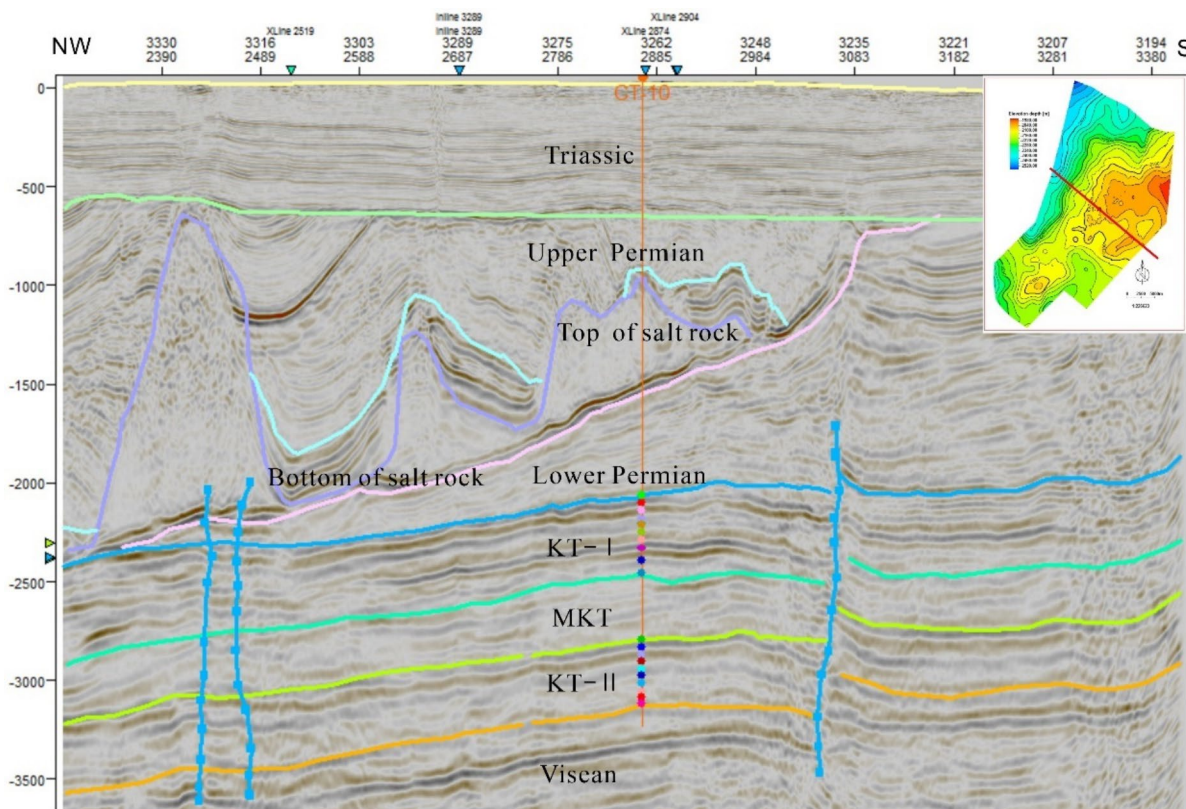

Fig. 3 Paleotectonic framework during the formation of the LAFs in the two-dimensional section
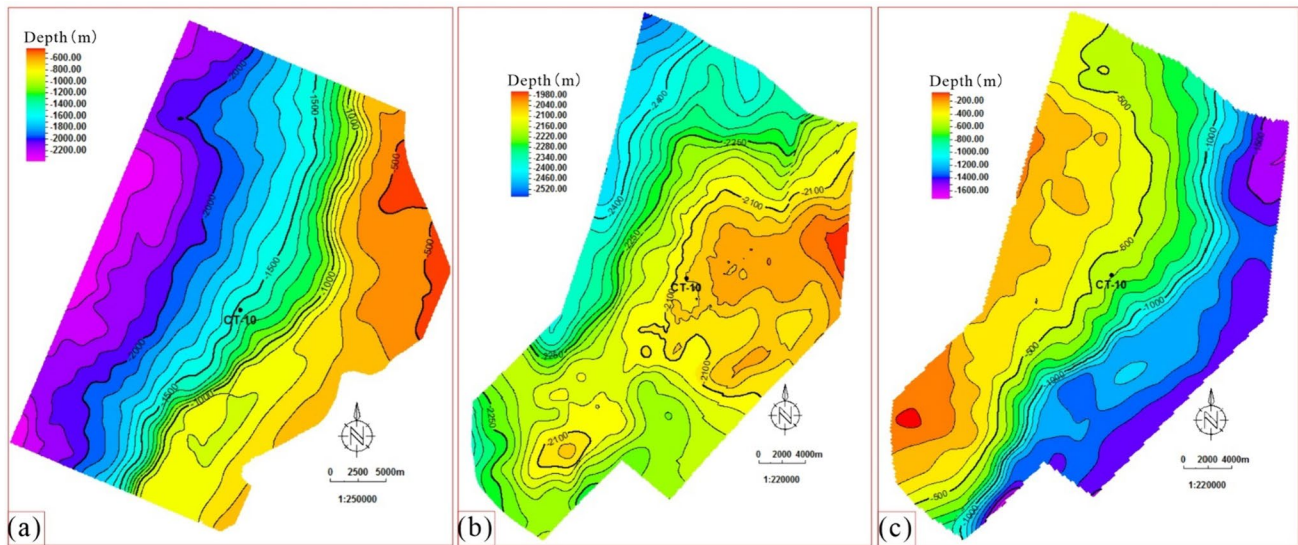
Fig. 4 Structural interpretation results based on seismic data of key horizons in the NT oilfield. **a** Seismic interpretation results of the present 3D structural map of top Permian surface; **b** seismic interpretation results of the present 3D structural map of the top surface of KT-I formation and **c** the 3D top structural map of KT-I formation during the formation of the low-angle fractures

The paleostructural restoration results based on seismic data suggested that the knee-fold structure developed in the study area during the formation of the low-angle fractures. The existence of the knee-fold structure in the study area during the formation of the LAFs can also be verified according to the coring data. The previous workers pointed out that the knee-fold structure generally develops interlayer peeling veins, flying-geese-like tensile veins, saddle veins and triangular veins based on the outcrops (Wang et al. 2014; Zheng and Mo 2007). Interlayer peeling veins, flying-geese-like tensile veins and triangular veins can be observed in the cores of the NT oilfield (Fig. 5), which further demonstrates that the knee-fold structure has developed in the study area. The knee-fold structure is a typical fault propagation fold.

Besides, the interlayer peeling veins, flying-geese-like tensile veins and triangular veins indicate that abnormally high pressure has developed in the study area. It has been pointed out in this paper that abnormally high pressure has no relationship with the hydrocarbon generation of organic matter in the study area, indicating that the abnormally high pressure in the study area is mainly related to the formation of water under the comprehensive influence of the knee-fold structure and the overlying salt stratum.

Analysis of in situ stress state types

Besides the influence of paleostructure on the formation of the low-angle fractures, the influence of the paleotectonic stress field also cannot be ignored; hence, it is necessary to study the in situ stress state types. Internationally, according to Anderson's stress classification scheme,

the geostress can be divided into three types: type Ia ($\sigma_z > \sigma_H > \sigma_h$), type II ($\sigma_H > \sigma_h > \sigma_z$) and type III ($\sigma_H > \sigma_z > \sigma_h$) (Burra et al. 2014; Sun et al. 2017a, b). The vertical distribution law of in situ stress state types in the world based on the previous studying results is that the buried depth of geostress type II is 0–500 m, the buried depth of geostress type III is 500–800 m and the buried depth of geostress type Ia is more than 800 m (Wang et al. 2000). However, some regions do not conform to this law, for example, the in situ stress of Fuyang oil layers in the Sanzhao area, Northeast China, is affected by horizontal tectonic compressive stress, and the vertical distribution law of in situ stress state types is as follows: When the buried depth is less than 1000 m, it belongs to type II in situ stress state, when the buried depth is 1000–1600 m, it belongs to type III in situ stress state and when it is greater than 1600 m, it belongs to type Ia in situ stress state (Wang et al. 2000). Based on the restoration results of paleostructure and the buried depth, this paper analyzes the types of in situ stress states in the study area.

Three-dimensional finite element method

To further analyze the mechanical mechanism of the low-angle fractures, this paper simulated the paleotectonic stress field during the formation of the low-angle fractures. Based on the paleostructural map in the formation of low-angle fractures, the tectonic geological model in the formation of the LAFs was established, and the rock mechanics attribute model was established according to
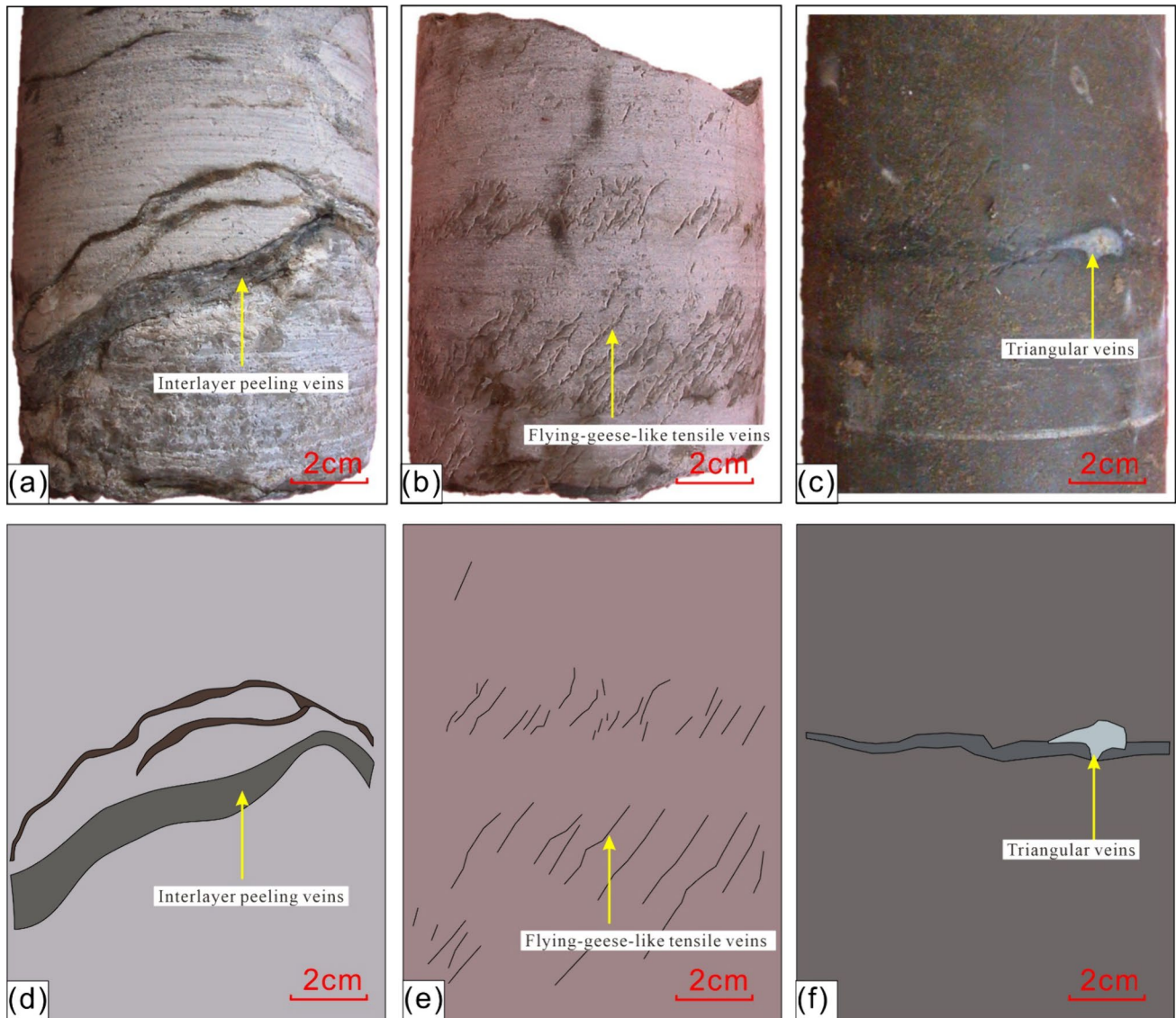
Fig. 5 Petrological evidence for the existence of knee band structure in the KT-I formation of the NT oilfield. **a** Interlayer peeling veins of well CT-10 with a depth of 2351.41 m. **b** Goose-like tensile vein of well CT-10 with a depth of 2393.75 m. **c** Triangular vein of well CT-10 with a depth of 2390.89 m. **d** Sketches of interlayer peeling veins of well CT-10 with a depth of 2351.41 m. **e** Sketches of goose-like tensile vein of well CT-10 with a depth of 2393.75 m. **f** Sketches of triangular vein of well CT-10 with a depth of 2390.89 m

the conventional logging data. The boundary conditions were determined by combining the above-mentioned geo-stress type analyzing results and the previous acoustic emission experimental results (Li et al. 2021). We used the Petrel/visage module to simulate the tectonic stress field during the formation of low-angle fractures. The simulation process of geostress field is shown in Fig. 6.

Establishment of structural modeling

The fault model was built according to the previous geological knowledge of the study area provided by the PetroChina Research Institute of Petroleum Exploration and Development, and only one NE–SW trending thrust fault developed in the east of the study area (Fig. 7a). The structural geological model was established based on the present 3D top structural surface of Permian and the present 3D top structural surface of KT-I formation. The plane grid size of the structural geological model is 300 m × 300 m, the vertical grid size is 7 m and the total number of geological grids is 399,600. The well spacing in the study area is 700 m, and the number of grids between wells is about 2, which can meet the requirements of simulation accuracy of in situ stress field (Fig. 7b). By flattening the 3D structural map of the Permian top surface, the paleostructural model of KT-I formation during the formation of the LAFs was established.
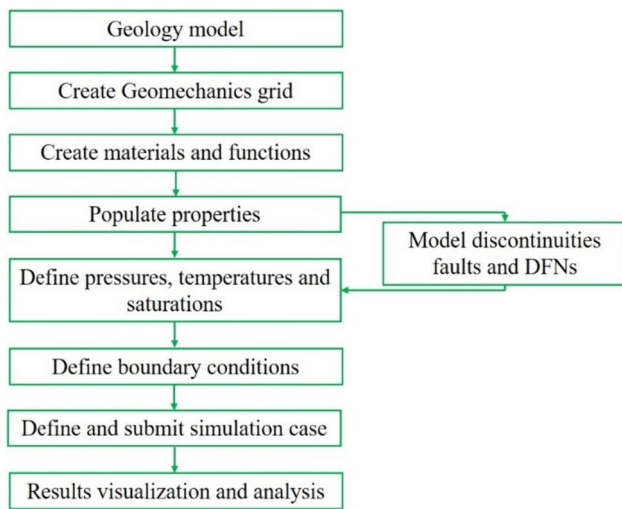
Fig. 6 Simulation process of geostress field

The structure of the KT-I formation during the formation of the LAFs is a typical kink-fold structure (Fig. 7c).

Modeling of rock mechanical properties

The key parameters such as elastic modulus, Poisson's ratio, uniaxial compressive strength, tensile strength, cohesion and internal friction angle of rock were calculated based on conventional logging data. The well needs to have both P-wave sonic interval transit time and S-wave sonic interval transit time to calculate parameters such as elastic modulus and Poisson's ratio. However, the well in the study area only measured the P-wave sonic interval transit time. To solve the problem of missing S-wave sonic interval transit time, the formula for calculating the S-wave sonic interval transit time based on the P-wave sonic interval transit time was adopted. The calculation formulas are shown in Table 1.

The elastic modulus and Poisson's ratio of rock obtained from conventional logging are dynamic mechanical parameters, which should be corrected according to static rock mechanical parameters. The static rock mechanical parameters can be obtained from rock experiments. Because the elastic modulus and Poisson's ratio of rock samples were not measured in the NT oilfield, and the rock mechanics experiments were carried out in Well 7001 and Well 8016 in the Kenkyak Oilfield adjacent to the NT oilfield (Fig. 1b); thus, the conversion of dynamic and static Young's modulus and dynamic and static Poisson's ratio was completed based on Well 7001 and Well 8016 in the Kenkyak Oilfield. The data of Young's modulus and Poisson's ratio interpreted by conventional logging have a good correlation with the data of Young's modulus and Poisson's ratio measured by rock experiments, which confirms the reliability of the fitting formula (Fig. 8). The calculation result of different rock mechanical parameters is shown in Fig. 9.

Based on the calculation results of single-well rock mechanical parameters, 3D attribute models of different rock mechanical parameters were established by using sequential Gaussian simulation. The idea of sequential Gaussian simulation is to generate a simulation path randomly, and then estimate the cumulative conditional distribution function of each point, and finally give the simulation value of this point according to the distribution function (Jika et al. 2020; Manchuk and Deutsch 2012). Note that the data used to calculate the cumulative conditional distribution function include both original data and simulated unconditional data. In the sequential Gaussian simulation process, it is necessary to determine the cumulative conditional distribution function of N univariates:

$$\begin{aligned}
&\text{Prob}\{Z_1 \leq z_1 | (n)\} \\
&\text{Prob}\{Z_2 \leq z_2 | (n+1)\} \\
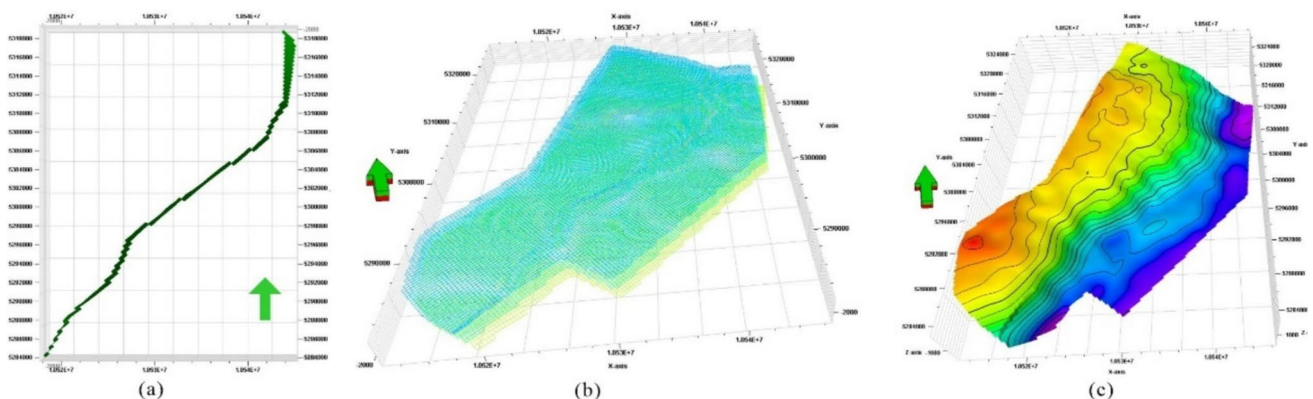&\text{Prob}\{Z_N \leq z_N | (n+N-1)\}
\end{aligned} \quad (1)$$

Fig. 7 Fault model and top structural model of the NT oilfield. **a** Fault model of the NT oilfield; **b** grid of the structural model of the NT oilfield and **c** top structural model of the NT oilfield

**Table 1** Formulas for calculating rock mechanical parameters by using conventional logging

Rock mechanical parameters	Formula
S-wave sonic interval transit time (Δt_s)	$\Delta t_s = \dfrac{\Delta t_p}{\left[1-1.15\,\frac{\frac{1}{\rho}+\left(\frac{1}{\rho}\right)^3}{e^{\frac{1}{\rho}}}\right]^{1.5}}$
Dynamic Young's modulus of rock (E)	$E = \dfrac{\rho\left(3\Delta t_s^2 - 4\Delta t_p^2\right)}{\Delta t_s^2\left(\Delta t_s^2 - \Delta t_p^2\right)} \times 9.29 \times 10^7$
Rock dynamic Poisson's ratio (μ)	$\mu = \dfrac{1}{2}\left(\dfrac{\Delta t_s^2 - 2\Delta t_p^2}{\Delta t_s^2 - \Delta t_p^2}\right)$
Shear modulus (G)	$G = \dfrac{\rho_b}{\Delta t_s^2} \times 9.29 \times 10^4$
Bulk modulus (K)	$K = G \times \dfrac{3\Delta t_s^2 - 4\Delta t_p^2}{3\Delta t_p^2}$
Coefficient of formation volume compressibility (C_b)	$C_b = \dfrac{1}{K_b} = \dfrac{3\Delta t_s^2 \Delta t_p^2}{\rho_b\left(3\Delta t_s^2 - 4\Delta t_p^2\right)}$
Skeleton volume compression coefficient (C_{ma})	$C_{ma} = \dfrac{1}{K_{ma}} = \dfrac{3\Delta t_{ms}^2 \Delta t_{mp}^2}{\rho_b\left(3\Delta t_{ms}^2 - 4\Delta t_{mp}^2\right)}$
Biot coefficient (α)	$\alpha = 1 - \dfrac{\rho_b\left(3v_p^2 - 4v_s^2\right)}{\rho_{ma}\left(3v_{map}^2 - 4v_{mas}^2\right)}$
Rock strength of carbonate rocks (S_C)	$S_C = E\left[0.008V_{sh} + 0.0045\left(1 - V_{sh}\right)\right]$
Tensile strength of rock (S_T)	$S_T = \dfrac{S_C}{12}$
Rock cohesion (C_0)	$C_0 = 5.44 \times 10^{-15}v_p^4\rho_b^2(1-2\mu) \times \left(\dfrac{1+\mu}{1-\mu}\right) \times \left(1 + 0.78V_{sh}\right)$
Internal friction angle of rock (φ)	$\varphi = 90 - \dfrac{360}{\pi}\tan^{-1}\left(\dfrac{1}{\sqrt{4.73-0.098\Phi}}\right)$

Remarks: Δt_s—S-wave sonic interval transit time, us/m; Δt_p—P-wave sonic interval transit time, us/m; ρ—Rock density, kg/m³; E—Dynamic Young's modulus, GPa; μ—Dynamic Poisson's modulus; G—Shear modulus, GPa; K—Bulk modulus, GPa; C_b—Coefficient of formation volume compressibility, GPa⁻¹; C_{ma}—Skeleton volume compression coefficient, GPa⁻¹; ρ_b, ρ_{ma}—Formation bulk density and rock skeleton bulk density, g/cm³; v_s, v_{mas}—Formation S-wave velocity and rock skeleton S-wave velocity, m/s; v_p, v_{map}—Formation P-wave velocity and rock skeleton P-wave velocity, m/s; Δt_{ms}—Rock skeleton S-wave sonic interval transit time, us/m; Δt_{mp}—Rock skeleton P-wave sonic interval transit time, us/m; V_{sh}—Clay content; S_C—Uniaxial compressive strength, GPa; S_T—Tensile strength of rock, GPa; C_0—Rock shear strength, GPa; φ—Rock internal friction angle, ° and Φ—Porosity, %

Sequential Gaussian simulation is a random simulation method that combines Gaussian probability theory and sequential simulation ideas. The prerequisite of sequential Gaussian simulation is that the variables meet the normal distribution characteristics, and if not, normal transformation is needed. In this study, the rock mechanical parameters predicted by using sequential Gaussian simulation can meet the normal distribution after transformation; thus, the rock mechanical parameters in the study area can be predicted by sequential Gaussian simulation

Fig. 8 Transformation of dynamic and static parameters of rocks in the KT-I formation of the NT oilfield. **a** The relationship between dynamic and static Young's modulus of rock and **b** the relationship between dynamic and static Poisson's ratio of rock
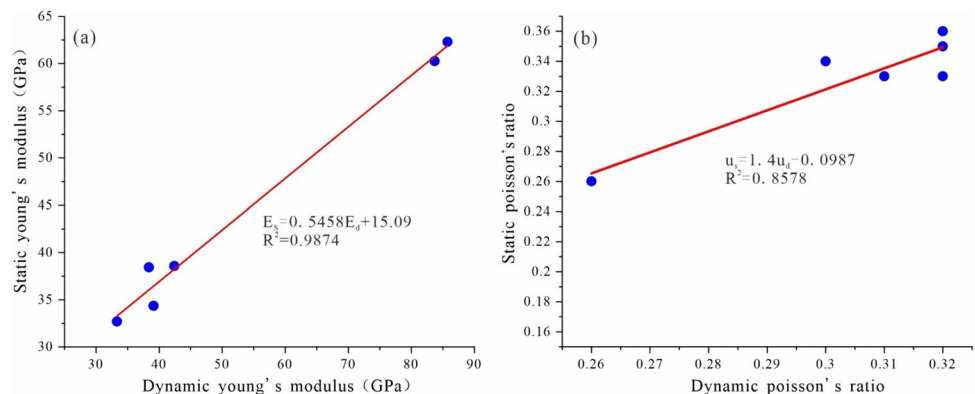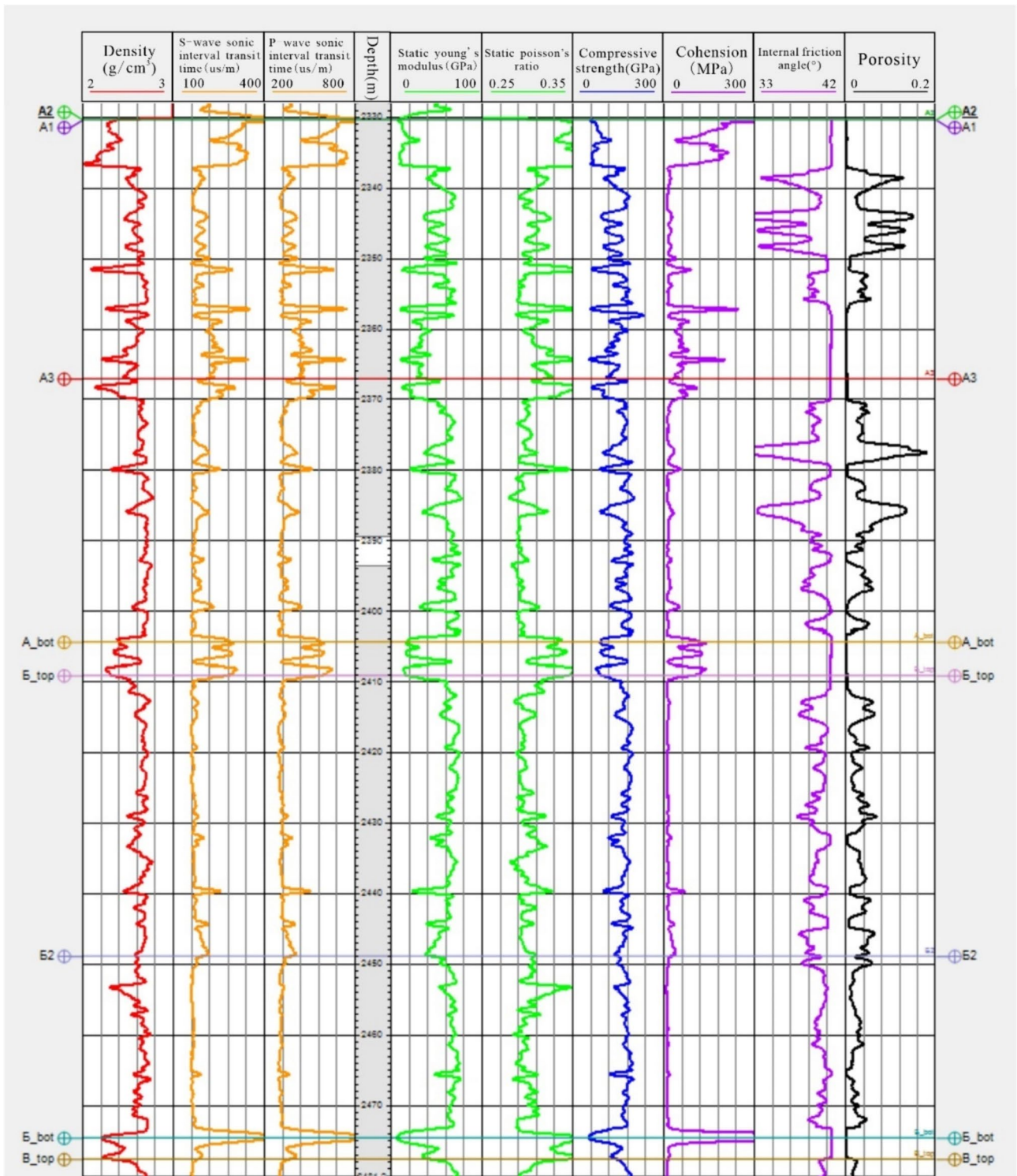
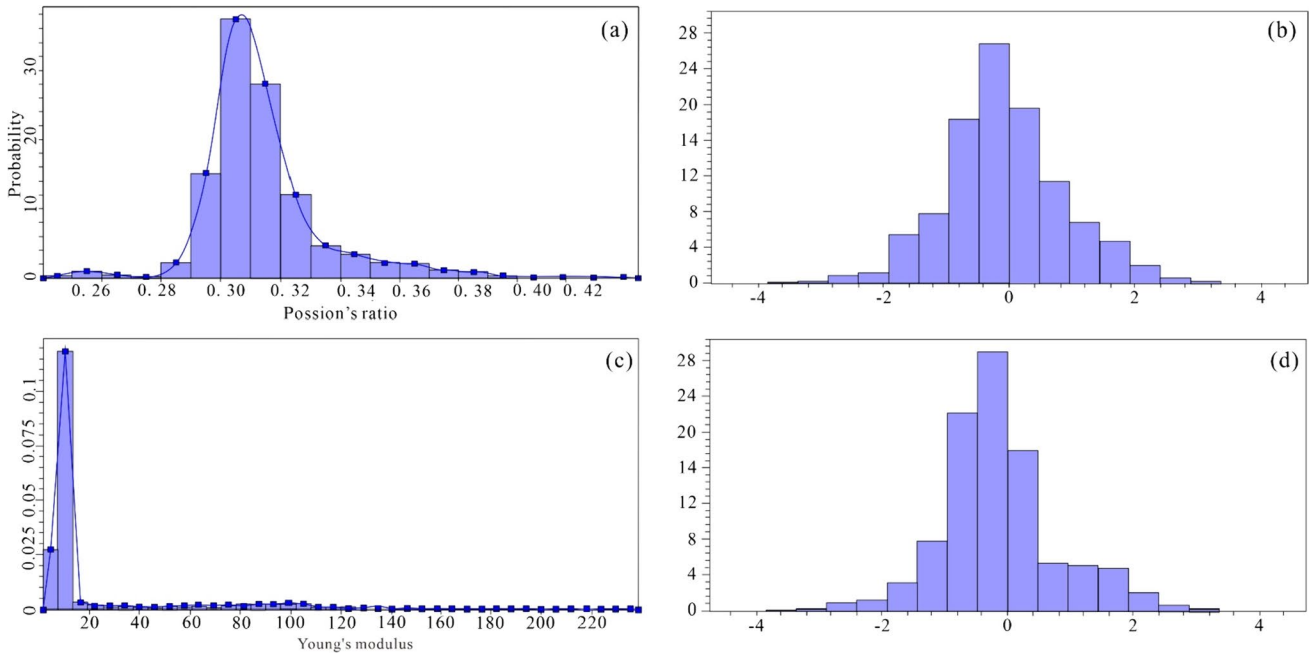**Fig. 9** Calculation results of different rock mechanical parameters of well CT-10 in the NT oilfield

Fig. 10 Normal distribution after transformation of Possion's ratio and Young's modulus in the NT oilfield. **a** Distribution of Possion's ratio data. **b** Normal distribution after transformation of Possion's ratio. **c** Distribution of Young's modulus data. **d** Normal distribution after transformation of Young's modulus

Fig. 11 Major search radius and minor search radius of Possion's ratio and Young's modulus in the NT oilfield. **a** Major search radius of Possion's ratio. **b** Minor search radius of Possion's ratio. **c** Major search radius of Young's modulus. **d** Minor search radius of Young's modulus
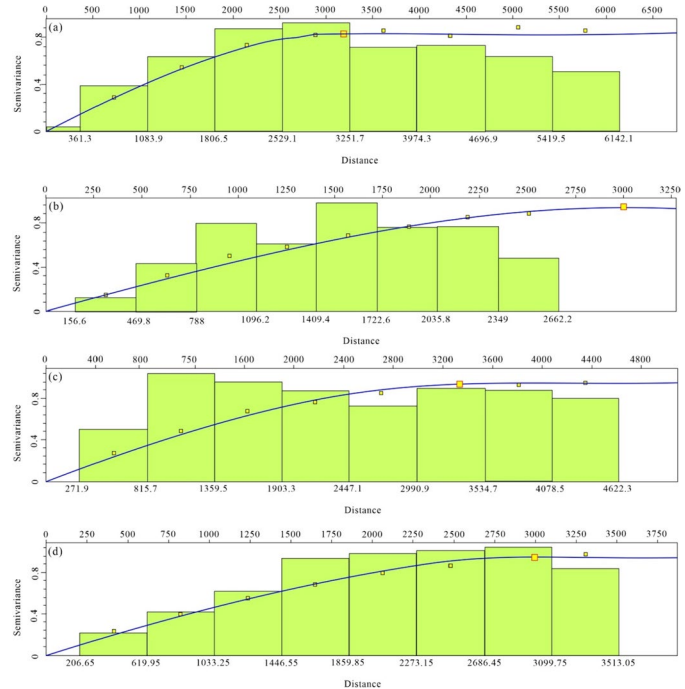
(Fig. 10) (Schmid 2018). In the process of simulating different rock mechanical properties in this study, it is considered that the rock mechanical properties are similar to those of sedimentary facies, and the major search radius and the minor search radius are 3300 m and 3000 m, respectively (Fig. 11). The direction of the major search radius is northeastern 27°. The prediction results of different rock mechanical parameters are shown in Fig. 12.
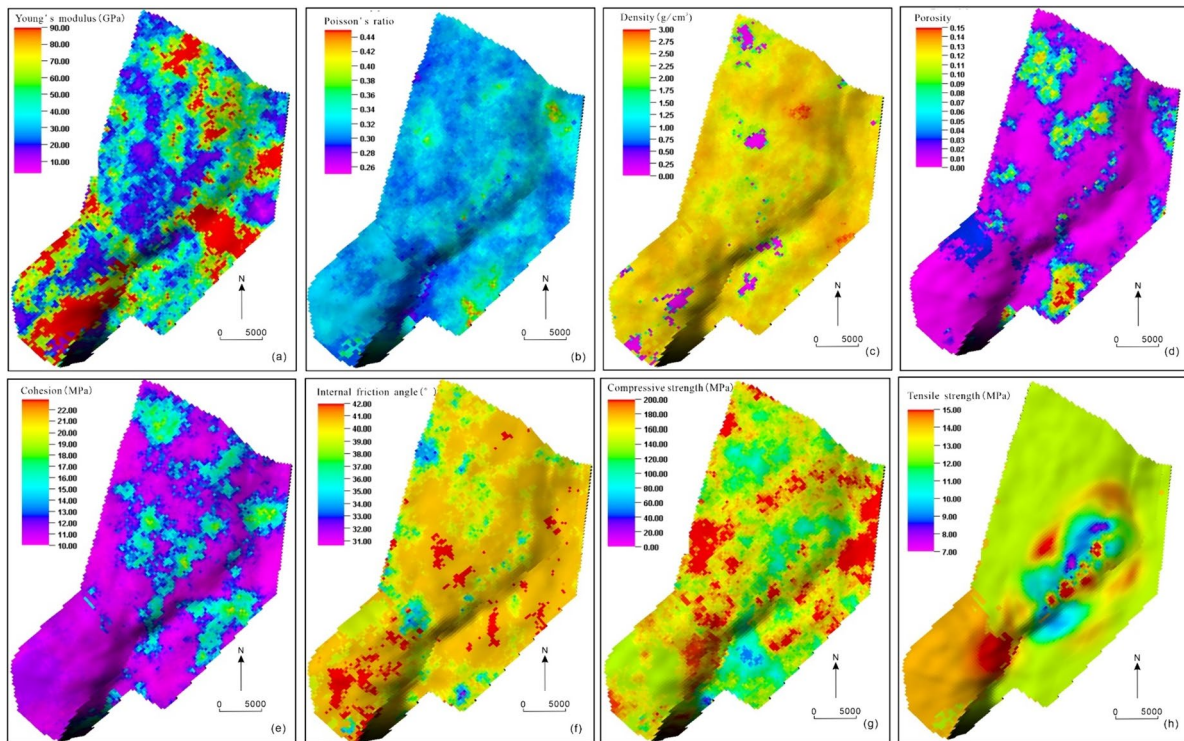
Fig. 12 Modeling results of different rock mechanical properties of KT-I formation in the NT oilfield. **a** Young's modulus attribute model; **b** Poisson's ratio attribute model; **c** density attribute model; **d** porosity attribute model; **e** cohesion attribute model; **f** attribute model of internal friction angle; **g** compressive strength attribute model and **h** tensile strength attribute mode
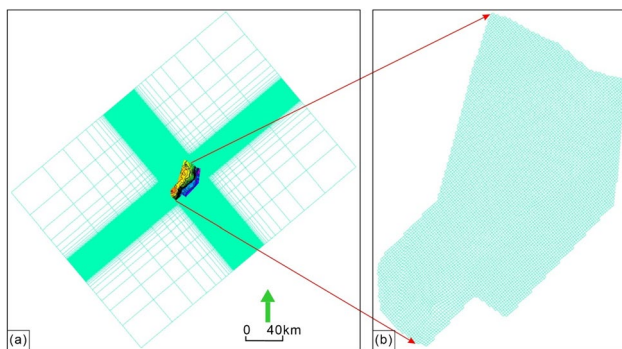

Fig. 13 Geomechanical grid of KT-I formation in the NT oilfield

Establishment of geomechanical grid

In order to accurately describe the in situ stress field in the study area, the geomechanical grid size is set to 300 m × 300 m, and the vertical size is set to 7 m, which is consistent with the structural model. To eliminate the influence of the boundary effect, the sideburden is multiplied by 3 times the area of the study area. And the geomechanical grid was rotated clockwise by 40° to press the boundary stress conveniently (Fig. 13).

Establishment of fault model in the geomechanical grid

The fault model is established when the structural model is built, thus the fault model is directly copied into the geomechanical grid from the structural model. However, it is necessary to set rock mechanical parameters for faults. The Young's modulus of the fault is 36 GPa, which is about 60% of the surrounding rock, and the Poisson's ratio is set to 0.35, which is 0.03 larger than the whole surrounding rock. The normal stiffness of the fault is 4000 MPa/m, and the tangential stiffness is 1500 MPa/m, and the cohesion is 0.001 MPa, and the internal friction angle is 20°, and the tensile strength is 0.001 MPa (Schmid 2018).

Determination of pore pressure of formation water

It is difficult to directly measure the actual pore pressure of formation water during the formation of the LAFs due to it only existed in the early upper Permian. Therefore, the pore pressure of formation water was speculated according to relevant evidence, and the speculated pore pressure of formation water was verified according to the simulation of the 3D geostress field. The formation pressure coefficient is defined as the ratio of the actual formation pressure to the hydrostatic pressure at the same depth. According to

the classification standard of formation pressure coefficient, a pressure coefficient greater than 1.1 is regarded as high pressure, and a pressure coefficient greater than 1.5 is regarded as ultra-high pressure (Du et al. 1995). The structure of the KT-I formation during the formation of the LAFs is a typical kink-fold structure (Fig. 4c). The previous studies have illustrated that kink-fold structures usually develop the overpressure (Mo et al. 2007; Zhang et al. 2010; Zheng and Mo 2007), and the coring data of the NT oilfield show the interlayer peeling veins with the aperture of 1 cm filled with calcite, which verifies the existence of fluid overpressure in the study area (Fig. 5a). Besides, the Kenkyak Oilfield, which is adjacent to the study area, is still developing overpressure at present, and the pressure coefficient is as high as 1.8, which demonstrated that the NT oilfield may develop ultra-high pressure in geological history (Wang 2012). Because oil and gas have not begun to charge during the formation of the low-angle fractures, the overpressure in the study area is mainly due to the existence of formation water under the influence of the overlaying salt stratum. The previous studies have suggested that the maximum formation pressure coefficient can reach 70–90% of the overburden pressure when abnormally high pressure develops (Zeng et al. 2007). Therefore, in order to simulate the pore pressure during the formation of the low-angle fractures, the formation pressure coefficient is set to 1.50, 2.00 and 2.43.

Determination of boundary conditions

In the process of in situ stress field simulation, the determination of boundary conditions is a key step, and the accuracy of boundary conditions directly determines whether the simulation results of the in situ stress field are reliable. Boundary conditions include vertical stress and horizontal stress. So far, the calculation method of vertical stress is relatively mature. Because the overburden pressure of rock is mainly formed by the weight of the overlying rock, vertical stress can be obtained through the density logging curve:

$$\sigma_v = \int_0^H \rho g \mathrm{d}z \tag{2}$$

where H is the buried depth of the target layer, m; ρ is the rock density, g/cm^3; g is the acceleration of gravity, m/s^2 and σ_v is the vertical stress, MPa. It is generally assumed that the rock density of the stratum is 2.7 g/cm^3, thus the above formula can be simplified as $\sigma_v = 0.027H$.

By comparing the vertical stress obtained from the rock samples test in the study area with the vertical stress calculated with the formula of $\sigma_v = 0.027H$, the results show that the error between the vertical stress obtained from the rock samples test in the NT oilfield and the vertical stress calculated with the formula of $\sigma_v = 0.027H$ is less than 0.1%, which confirms the reliability of the vertical stress calculated with the formula of $\sigma_v = 0.027H$ in the study area (Table 2).

Many calculation models were put forward to calculate the horizontal stress (Qiu 2017). Different calculation models can be divided into two categories. The first category is the uniaxial strain empirical model, which assumes that the rock is mainly subjected to vertical stress, and the horizontal deformation of layered rock is limited, thus the rock only undergoes vertical deformation. This kind of model includes the Dinnik empirical model, the Mattews and Kelly model, the Terzaghi model, the Aderson model, the Newberry model, etc. The empirical model of uniaxial strain only considers the vertical deformation of strata, and it does not consider the horizontal deformation of strata, which is not consistent with reality. The second category is the multi-axial strain empirical model, including Huang's model, combined spring model, porous elastic horizontal strain model, Schlumberger model and ADS model. Though the combined spring model ignores the anisotropic characteristics of rocks, it is convenient and in good agreement with the reality for carbonate rocks, thus it is a common horizontal stress model for predicting paleotectonic stress field (Ostadhassan et al. 2012; Thiercelin and Plumb 1994). The combined spring model mainly simulates the in situ stress field by determining the strain boundary conditions.

Petrel/visage software provides two ways to apply boundary conditions: the stress model and the strain model. The stress model simulates the initial stress using the stress given at the boundary and the strain method simulates the initial stress using the strain given at the boundary. Therefore, this

Table 2 Comparison between theoretically calculated vertical geostress and actually measured geostress of rocks in the NT oilfield

Well	Sample number	Formation	Depth	Measured vertical stress (MPa)	Vertical stress by theoretical calculation (MPa)	Error (%)
CT-10	R2008-08818-8a	KT-I	2346.90	63.36	63.3663	0.0099
CT-10	R2008-09020-7	KT-II	3121.84	84.29	84.2896	0.0004
CT-10	R2008-09125-8a	KT-II	3155.90	85.21	85.2093	0.0008
CT-10	R2008-09213-7	KT-II	3189.40	86.11	86.1138	0.0044

study mainly determines the strain boundary conditions of the study area and applies the combined spring model theory to realize the simulation of the in situ stress field.

The strain boundary conditions can be obtained by the acoustic emission experimental results. The acoustic emission experimental results show that the maximum principal stress during the formation of the LAFs in the study area is $\sigma_H = 42.4$ MPa (Li et al. 2021). Note that the maximum principal stress here is the effective maximum principal stress, and the total maximum principal stress should add the maximum principal stress and the hydrostatic pressure which can be calculated according to the buried depth of the rock samples' testing point.

The present buried depth of the rock samples' testing point is 2346.9 m. By analyzing the elastic modulus and Poisson's ratio of rock calculated by logging curves at this depth, it is known that the elastic modulus is $E = 50$ MPa, and Poisson's ratio is $\mu = 0.3$. The buried depth of rock samples testing the acoustic emission experiment is 604 m during the formation of the low-angle fractures, thus the hydrostatic pressure at the testing point for the acoustic emission experiment is $P_p = 6.04$ MPa during the formation of the low-angle fractures. Because the pore pressure coefficient of formation water is set to 1.50, 2.00 and 2.43 in this study, the total maximum horizontal principal stress is 51.46 MPa, 54.48 MPa and 57.08 MPa (Table 3). According to the total maximum principal stress in the study area and the combined spring model and the previous analysis results of horizontal strain under a similar structural background in Australia (Tavener et al. 2017), the strain values in the direction of maximum principal stress and minimum principal stress were determined, respectively (Table 3).

Rock rupture theory

To determine the conditions of brittle rupture of rocks, the previous workers studied tensile failure and shear failure, respectively, and established a variety of rupture criteria, such as the Griffith criterion and tensile failure criterion, especially for tensile failure, and Coulomb–Moore criterion and Drucker–Prager criterion especially for shear failure

(Liu 2015, 2010). So far, the most classical rock fracture criteria for brittle fracture are the Griffith criterion for tensile failure and the Coulomb–Moore criterion for shear failure. In addition, for rocks with weak fabrics, the previous workers built the non-coordination criterion. The following introduces the Griffith criterion, Coulomb–Moore criterion and non-coordination criterion in detail.

Griffith criterion

Griffith's criterion mainly focuses on tensile fracture. This theory was originally used to explain the mechanism of glass breakage and was subsequently introduced into the study of rock rupture. Griffith's criterion holds that there are a large number of tiny fractures in the rock before the external force is applied. When the external force is applied to the rock, stress concentration will occur around the tiny fractures, and the tiny fractures in the rock will begin to expand under the external force and form tensile fractures.

The precondition of rock tensile fracture is that the minimum principal stress is tensile. In the study of rock mechanics, it is stipulated that the compressive stress of rock is positive and the tensile stress is negative, thus the application condition of tensile fracture is that the minimum principal stress is less than zero. Griffith's criterion can be divided into two situations when applied:

If $(\sigma_1 + 3\sigma_3) > 0$;

$$(\sigma_1 - \sigma_2)^2 + (\sigma_2 - \sigma_3)^2 + (\sigma_3 - \sigma_1)^2 = 24(\sigma_1 + \sigma_2 + \sigma_3)\sigma_T \tag{3}$$

Namely:

$$\sigma_T = \frac{(\sigma_1 - \sigma_2)^2 + (\sigma_2 - \sigma_3)^2 + (\sigma_3 - \sigma_1)^2}{24(\sigma_1 + \sigma_2 + \sigma_3)} \tag{4}$$

$$\cos 2\beta = \frac{\sigma_1 - \sigma_3}{2(\sigma_3 + \sigma_1)} \tag{5}$$

If $(\sigma_1 + 3\sigma_2) \leq 0$;

Table 3 Boundary conditions for different pore pressure coefficients of formation water

Pore pressure coefficient	1.00	1.50	2.00	2.43
Pore pressure (MPa)	6.04	9.06	12.08	14.68
Vertical stress gradient (MPa/m)	0.027	0.027	0.027	0.027
Hydrostatic pressure gradient (MPa/m)	0.0100	0.0150	0.0200	0.0243
Ratio of the hydrostatic pressure gradient to vertical geostress gradient	0.3704	0.5556	0.7407	0.9000
Total maximum principal stress (MPa)	48.44	51.46	54.48	57.08
Strain value in the direction of maximum principal stress	0.00060	0.00065	0.00070	0.00075
Minimum principal stress direction strain value	0.00012	0.00013	0.00014	0.00015

Fig. 14 Schematic diagrams of rock stress and Coulomb–More criterion. **a** Rock stress diagram of the unit body and **b** Coulomb–More criterion diagram

$$\sigma_T = -\sigma_3 \tag{6}$$

$$\sin 2\beta = 0 \tag{7}$$
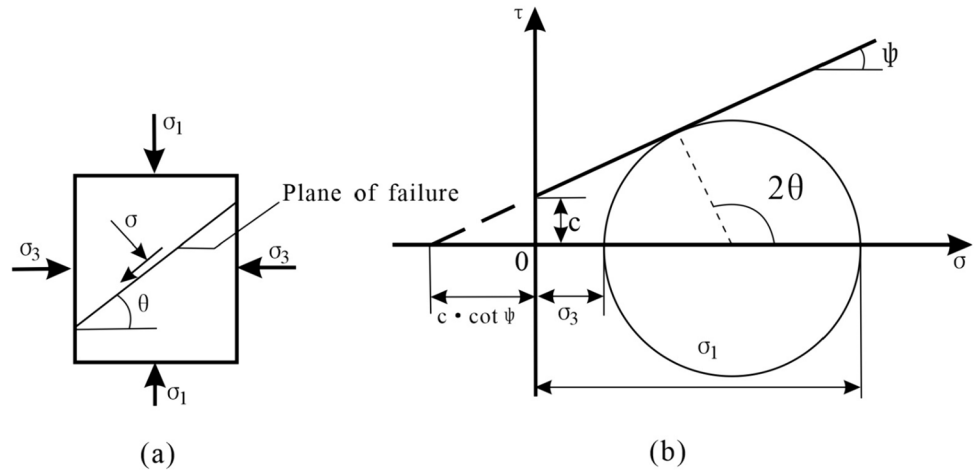
where β is the internal friction angle. σ_1 is the first principal stress, MPa; σ_2 is the second principal stress, MPa; σ_3 is the third principal stress, MPa and σ_T is the critical rupture pressure, MPa. In this situation, the direction of tensile fracture in rock is along the propagation direction of the maximum principal stress σ_1.

Coulomb–Moore criterion

The Coulomb–Moore criterion is mainly applicable to shear fracture. This theory holds that the rupture of rock is due to the existence of shear action on a certain surface of rock, which exceeds the strength of shear rupture of rock (Fig. 14). The expression in the process of rock rupture can be written as follows:

$$\tau_n = C + \delta_n \tan \varphi \tag{8}$$

where C is the shear strength of the rock; $\tan \varphi$ is the coefficient of internal friction in the rock and φ is the internal friction angle of the rock.

When the value on the right side of the formula is greater than that on the left side in formula (8), the rock mass will form a fracture. The above relationship can be expressed in the Cartesian coordinate system. Taking the compressive stress on the rock as the abscissa and the shear stress as the ordinate, as shown in Fig. 14b, the above formula is a straight line in the Cartesian coordinate system. When half of the difference between the maximum principal stress and the minimum principal stress is tangent or intersects with the straight line, the rock can be ruptured (Fig. 14).

The σ and τ in the coordinate system can be obtained by the following formula:

$$\sigma = \frac{1}{2}(\sigma_1 + \sigma_3) + \frac{1}{2}(\sigma_1 - \sigma_3) \cos 2\theta \tag{9}$$

$$\tau = \frac{1}{2}(\sigma_1 - \sigma_3) \sin 2\theta \tag{10}$$

where σ_1 is the maximum principal stress, and σ_3 is the minimum principal stress. θ is the included angle between the failure surface and the direction of σ_3, namely, the included angle between the normal of the failure surface and the direction of σ_1.

After transforming the above formula, the criterion can be expressed by using σ_1 and σ_3, and it can be rewritten as follows:

$$\frac{(\sigma_1 - \sigma_3)}{\sigma_1 + \sigma_3 + 2c \cot \varphi} = \sin \varphi \tag{11}$$

$$\sigma_1 = \sigma_3 V_\varphi + S_c \tag{12}$$

$$V_\varphi = \cot 2\left(45° - \frac{\varphi}{2}\right) \tag{13}$$

$$S_c = 0.035 V_p - 31.5 \tag{14}$$

where S_c is the compressive strength, and V_p is the shear wave velocity, m/s.

Non-coordination criterion

Underground rocks are heterogeneous. Due to factors such as bedding or foliation, pre-existing weak fabrics often develop in rocks. Tong et al. (2011) deduced the shear fracture criterion of rock when developing pre-existing weak fabrics,
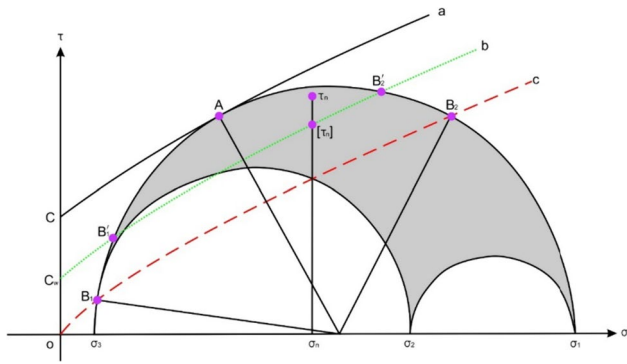
Fig. 15 Mohr circle diagram of triaxial stress for non-coordination criterion. **a** Rupture envelope for intact rock; **b** rupture envelope for rock with weak fabrics and **c** line of fault activity (Tong et al. 2011)

which is known as the non-coordination criterion. The rupture coefficient of weak fabrics can be defined as follows:

$$f_{aw} = \frac{\tau_n}{[\tau_n]} \tag{15}$$

where τ_n is the shear stress of the weak fabrics, and $[\tau_n]$ is the shear stress corresponding to the same normal stress on the rupture line. The pre-existing weak fabrics of rock with $f_{aw} = 1$ are in a critical breakage state, the pre-existing weak fabrics with $f_{aw} > 1$ are in a breakage state, the pre-existing weak fabrics with $f_{aw} < 1$ are below the rupture line and the pre-existing weak fabrics do not develop fractures (Fig. 15).

When the magnitude and direction of the three principal stresses are determined, the normal stress (σ_n) and shear stress (τ_n) on any interface in space are as follows, respectively:

$$\sigma_n = \left(\sigma_1 \sin^2\theta + \sigma_2 \cos^2\theta \cos^2\alpha + \sigma_3 \cos^2\theta \sin^2\alpha\right) \tag{16}$$

$$\tau_n = \sqrt{\sigma^2 - \sigma_n^2} \tag{17}$$

where θ is the angle between the weak fabrics and the direction of σ_1, and α is the angle between the intersection of the weak fabrics on the σ_2–σ_3 plane and the minimum principal stress σ_3.

$$\sigma^2 = \sigma_1^2 \sin^2\theta + \sigma_2^2 \cos^2\theta \cos^2\alpha + \sigma_3^2 \cos^2\theta \sin^2\alpha \tag{18}$$

According to the rock rupture criterion:

$$[\tau_n] = C_W + \mu_w \times \sigma_n \tag{19}$$

The fracture coefficient of any weak fabric is

$$f_{aw} = \frac{\sqrt{\sigma^2 - \sigma_n^2}}{C_W + \mu_w \times \sigma_n} \tag{20}$$

If the stress state, the shear strength C_W, the internal friction coefficient μ_w and the occurrence of the pre-existing weak fabrics are known in advance, the fracture coefficient f_{aw} of the pre-existing weak fabrics can be calculated quantitatively.

When $C_W = 0$ and μ_w is replaced by f_F, the activity coefficient f_{aF} of the pre-existing fault can be obtained.

$$f_{aF} = \frac{\sqrt{\sigma^2 - \sigma_n^2}}{f_F \times \sigma_n} \tag{21}$$

The above formula unifies the activity coefficient f_{aF} of pre-existing faults to the fracture coefficient f_{aw} of pre-existing weak fabrics. The pre-existing fault activity coefficient (f_{aF}) and pre-existing weak fabrics activity coefficient (f_{aw}) are collectively called the pre-existing structural activity coefficient (f_{aS}).

When $C_W = C$ (equivalent to homogeneous body), the gray shaded part in Fig. 15 shrinks to a point (A), and the included angle between the corresponding section and the direction of σ_1 is $\theta = 45° + \varphi/2$, which is perpendicular to σ_3 (namely, $\alpha = 90$). Figure 15 shows that only the activity coefficient of point A is 1, and others are less than 1. According to the condition of point A ($\alpha = 90°$, $\theta = 45°-\varphi/2$) and isotropic body ($C_W = C$, $\mu_w = \tan\varphi$), it can be obtained:

$$f_{aw} = \frac{\sqrt{\left(\sigma_1^2 \sin^2\theta + \sigma_3^2 \cos^2\theta\right) - \left(\sigma_1 \sin^2\theta + \sigma_3 \cos^2\theta\right)^2}}{C + \tan\varphi \times \left(\sigma_1 \sin^2\theta + \sigma_3 \cos^2\theta\right)} = 1 \tag{22}$$

After further simplification, it can be obtained:

$$\tau_n = C + \tan\varphi \times \sigma_n \tag{23}$$

where

$$\tau_n = \sqrt{\left(\sigma_1^2 \sin^2\theta + \sigma_3^2 \cos^2\theta\right) - \left(\sigma_1 \sin^2\theta + \sigma_3 \cos^2\theta\right)^2} \tag{24}$$

$$\sigma_n = \sigma_1 \sin^2\theta + \sigma_3 \cos^2\theta \tag{25}$$

It can be seen that the isotropic body's Coulomb–Moore criterion is only a special case of the non-coordination criterion.

Fig. 16 Fractures with different mechanical properties in the cores of KT-I formation of the NT oilfield. **a** Shear fracture in the cores of the well CT-4 with a depth of 2294.90 m and **b** tensile fracture in the cores of the well CT-22 with a depth of 2395.58 m
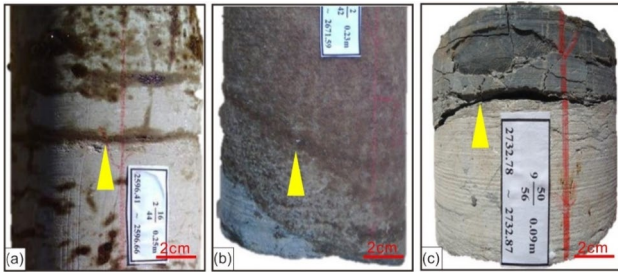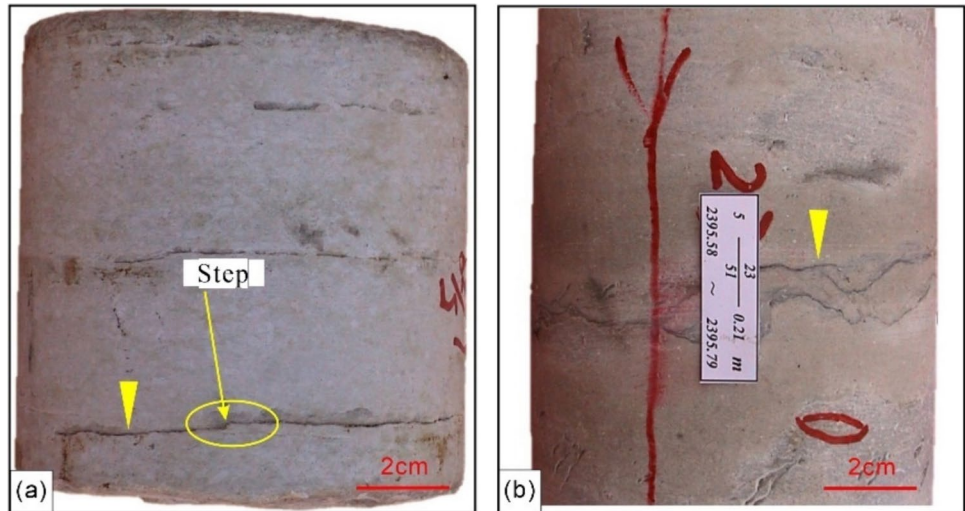

Fig. 17 Characteristics of LAFs in cores of the KT-I formation of the NT oilfield. **a** Near-horizontal LAFs in the non-weak fabrics section of the well CT-64 with a depth of 2596.41–2596.66 m; **b** the LAFs having a certain angle with bedding in the non-weak fabrics section of the well CT-64 with the depth of 2671.36–2671.59 m and **c** near-horizontal LAFs in the weak fabrics section of the well CT-64 with a depth of 2732.78–2732.87 m

Results

Types and filling characteristics of low-angle fractures

Types of low-angle fractures

Fractures can be divided into shear fractures and tensile fractures according to their mechanical properties. The occurrence of the shear fracture is stable and extending far away, and the wall of the shear fracture is flat and smooth, occasionally developing scratches and steps (Fig. 16a). The occurrence of tensile fractures is unstable and does not extend far, and the wall of tensile fractures is rough, short and curved, without scratches and steps (Fig. 16b). The NT oilfield mainly developed shear fractures, making up for 90.2%, and tensile fractures only account for 9.8%.

According to the dip angle of LAFs and the beddings in rocks, the low-angle shear fractures in the study area can be further divided into three types, including near-horizontal LAFs in the non-weak fabrics section (type I low-angle shear fractures), LAFs having a certain angle with bedding in the non-weak fabrics section (type II low-angle shear fractures) and near-horizontal LAFs in the weak fabrics section (type III low-angle shear fractures) (Fig. 17). It can be seen that the fracture of type I and type II low-angle shear fractures is almost unaffected by beddings, while the development of type III low-angle shear fractures has a certain relationship with rock beddings.

Filling characteristics of low-angle fractures

Fractures can be divided into unfilled fractures, partially filled fractures and filled fractures according to the fracture filling degree. Based on the core data, the filling characteristics of LAFs in the study area were analyzed. The results show that the LAFs in the NT oilfield are mainly unfilled fractures, with a percentage of the number of 65.0%, and the proportion of the number of partially filled fractures is 18.9%, and the proportion of the number of fully filled fractures is 16.1% (Fig. 18a). The fillings of LAFs in the study area are mainly argillaceous, with occasional fillings such as asphalt, siliceous, calcite and dolomite (Fig. 18b).

Based on the core data, the filling characteristics of LAFs with different mechanical properties were further studied. The results illustrate that shear fractures are chiefly the unfilled fractures, with a proportion of the number of 70.9%, while the tensile fractures are primarily the unfilled
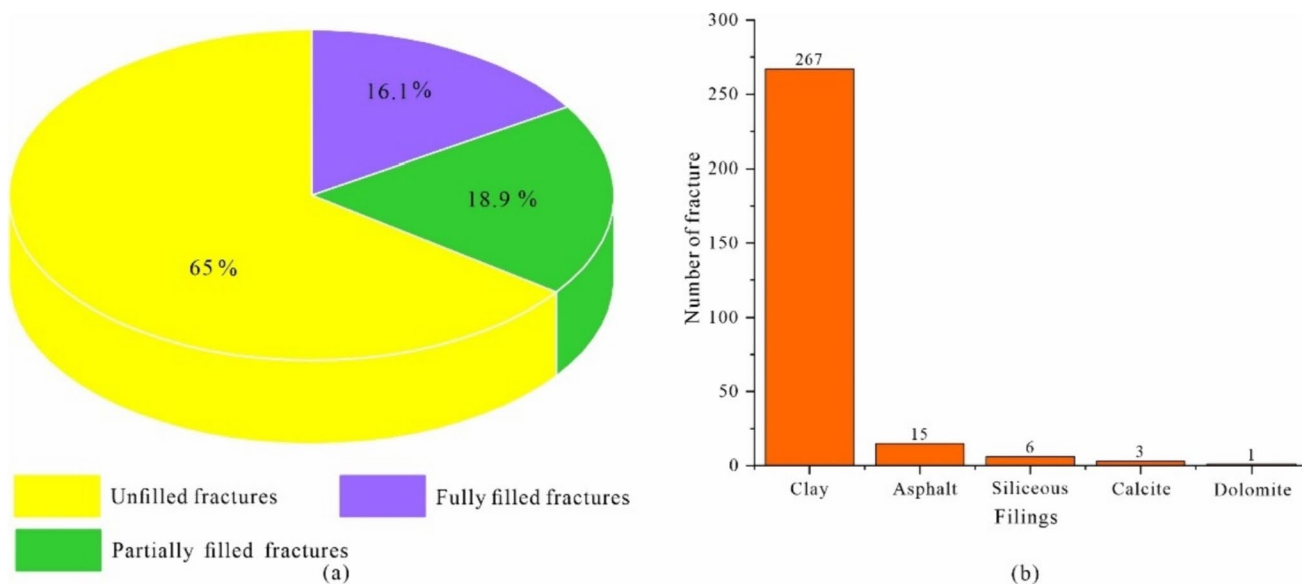
Fig. 18 Percentage of the number of LAFs with different fillings and fillings characteristics of cores in the KT-I formation of the NT oilfield. **a** Percentage of the number of the LAFs with different fillings and fillings characteristics of cores in the KT-I formation of the NT oilfield (*N* = 834) and **b** the number of fractures with different fillings of cores in the KT-I formation of the NT oilfield

Fig. 19 Filling characteristics of LAFs with different mechanical properties in cores of the KT-I formation of the NT oilfield. **a** Filling characteristics of shear fractures in cores of the KT-I formation of the NT oilfield (*N* = 752) and **b** filling characteristics of tensile fractures in cores of the KT-I formation of the NT oilfield (*N* = 82)
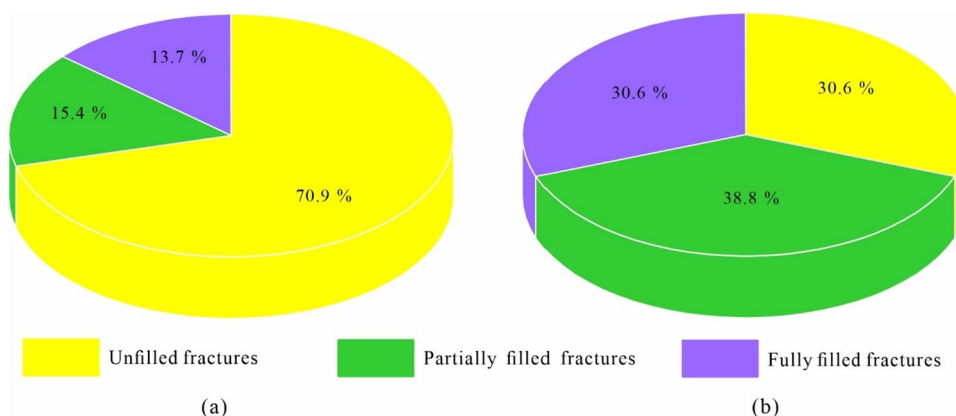
fractures, and the percentage of the number of unfilled tensile fractures is only 30.6% (Fig. 19a and b). The filling degree of tensile fractures is higher than that of shear fractures, mainly due to the larger aperture of tensile fractures leading to greater fluid flux and easier precipitation of cement.

Analysis of in situ stress types

The buried depth of most parts of the KT-I formation is less than 800 m, and the thrust faults are developed during the formation of the LAFs in the study area, which displays that the tectonic setting of the study area is horizontal compression, and the vertical stress is relatively small. Therefore, the in situ stress type of the study area

during the formation of the LAFs is type II. The example of the Fuyang oil layers in the Sanzhao area confirms the rationality of determining the in situ stress types in the study area as type II. Besides, the buried depth of the strata in the first tectonic movement is less than that in the second tectonic movement, which suggests that the in situ stress in the first tectonic movement is also type II. The third tectonic movement in the study area occurred in the late Permian, and the Kungurian salt formation deposits during this time. The average thickness of the Kungurian salt formation is about 150 m in the study area (Jing 2021), that is, the thickness of the overburden stratum of the KT-I formation is 950 m. Because the third tectonic movement was caused by Ural orogeny and developed structural inversion, which confirmed that the third tectonic
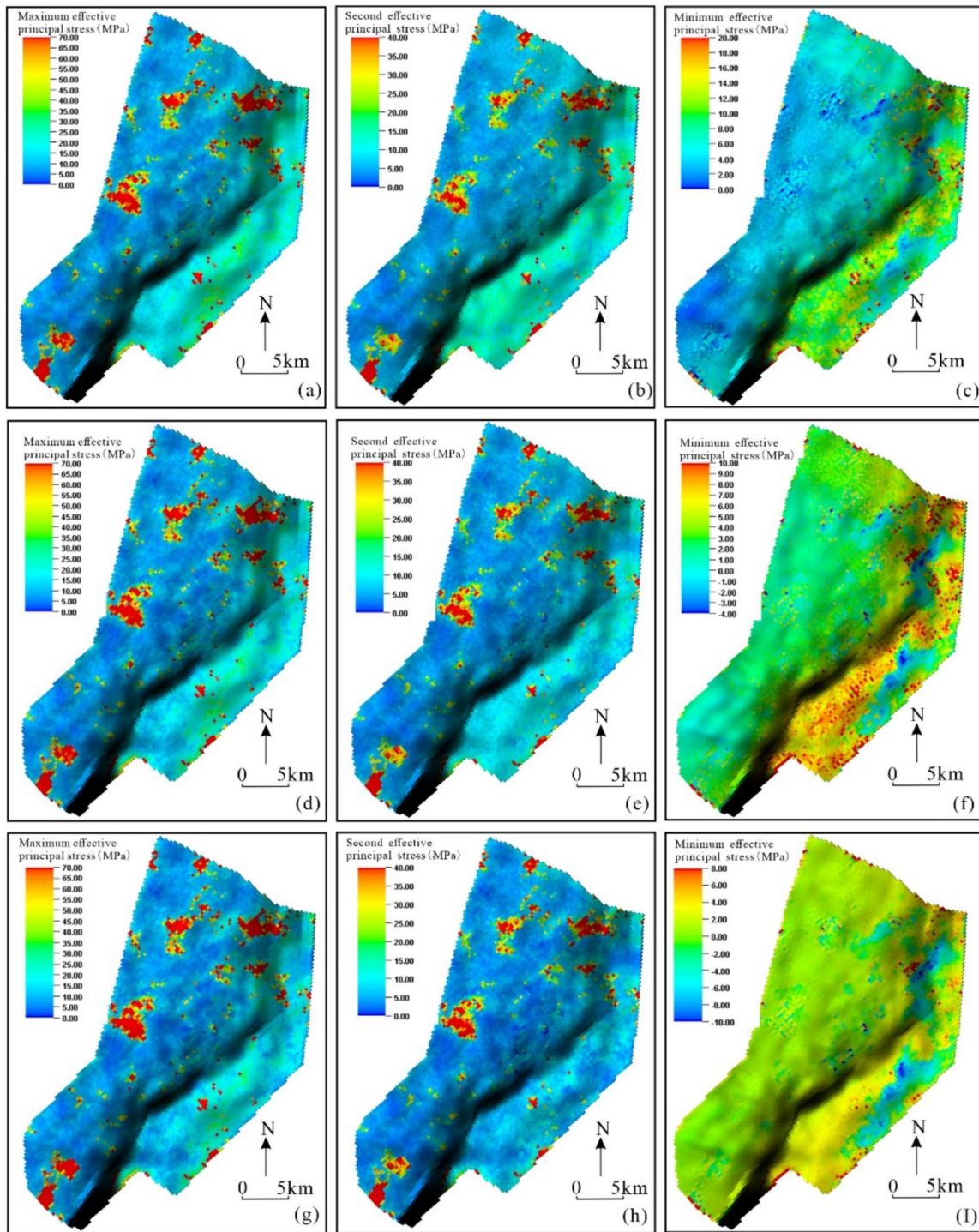
Fig. 20 Simulation results of in situ stress field for different formation pressure coefficients of KT-I formation in the NT oilfield. **a** The first principal stress distribution when the formation pressure coefficient is 1.50; **b** the second principal stress distribution when the formation pressure coefficient is 1.50 and **c** the third principal stres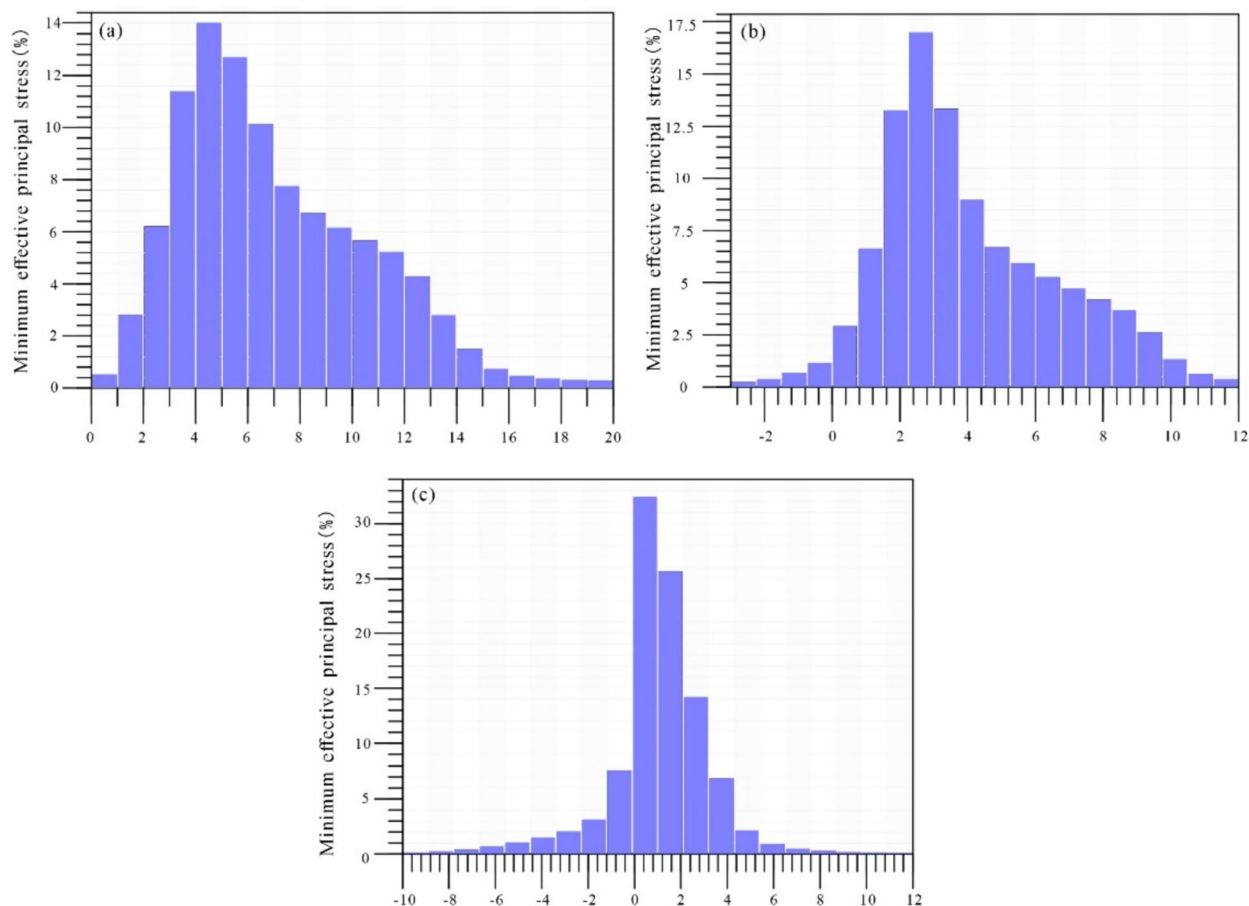s distribution when the formation pressure coefficient is 1.50; **d** the first principal stress distribution when the formation pressure coefficient is 2.00; **e** the second principal stress distribution when the formation pressure coefficient is 2.00 and **f** the third principal stress distribution when the formation pressure coefficient is 2.00; **g** the first principal stress distribution when the formation pressure coefficient is 2.43; **h** the second principal stress distribution when the formation pressure coefficient is 2.43 and **i** the third principal stress distribution when the formation pressure coefficient is 2.43

Fig. 21 Distribution of minimum principal stress for different formation pressure coefficients in KT-I formation of the NT oilfield. **a** Distribution of minimum principal stress when the formation pressure coefficient is 1.50; **b** distribution of minimum principal stress when the formation pressure coefficient is 2.00 and **c** distribution of minimum principal stress when the formation pressure coefficient is 2.43

movement in the study area was characterized by strong horizontal stress, thus the stress type of the third tectonic movement was also regarded as type II.

Analysis of stress field simulation results

By simulating the stress field with different formation pressure coefficients, the results show that when the formation pressure coefficient is 1.50, the maximum principal stress is 0–70 MPa, the intermediate principal stress is 0–40 MPa, and the minimum principal stress is 0–30 MPa (Fig. 20a–c). When the formation pressure coefficient is 2.00, the maximum principal stress is 0–70 MPa, the intermediate principal stress is 0–40 MPa, and the minimum principal stress is − 4–10 MPa (Fig. 20d–f). When the formation pressure coefficient is 2.43, the maximum principal stress is 0–70 MPa, the intermediate principal stress is 0–40 MPa and the minimum principal stress is

− 10–8 MPa (Fig. 20g–i). Obviously, with the enhancement of abnormally high pressure, the proportion of tensile stress in the study area is increasing, that is, tensile fractures are more developed.

When the formation pressure coefficient is 1.50, the minimum principal stress values are all positive, that is, compressive stress, which is difficult to explain the existence of the tensile fractures in the study area (Fig. 21a). When the formation pressure coefficient is 2.00, the percentage of the tensile stress of the minimum principal stress is only about 2.6%, which is still difficult to explain the geological phenomenon that the percentage of the number of tensile fractures in the study area is as high as 9.8% (Fig. 21b). When the formation pressure coefficient is 2.43, the percentage of the tensile stress of the minimum principal stress is 9.8%, which is consistent with the geological phenomenon that the percentage of the number of core tensile fractures in the study area is 9.8% (Fig. 21c). Therefore, it is determined that
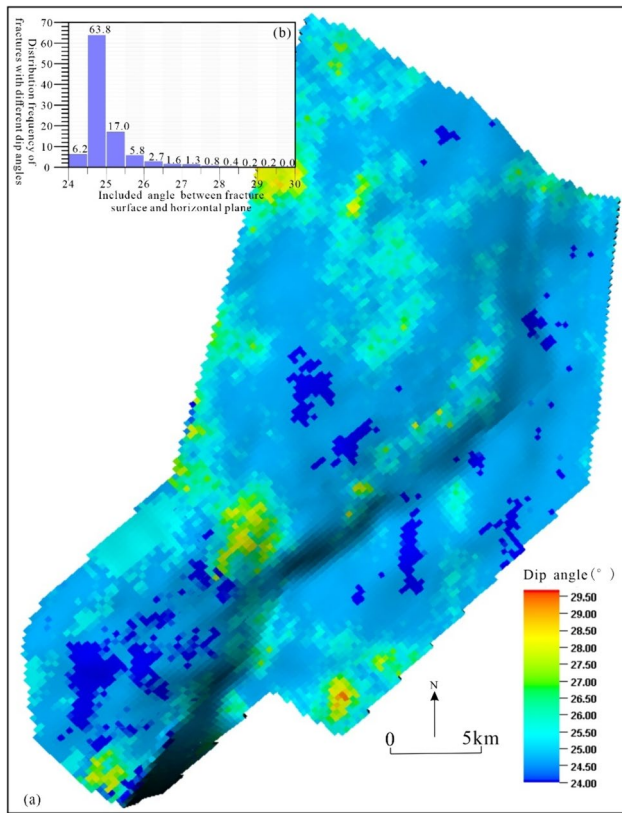
**Fig. 22** The 3D attribute model and distribution of the included angle between low-angle shear fracture and horizontal plane in KT-I formation of the NT oilfield. **a** The 3D attribute model of the included angle between low-angle shear fracture and horizontal plane in KT-I formation of the NT oilfield and **b** distribution of the included angle between low-angle shear fracture and horizontal plane in KT-I formation of the NT oilfield
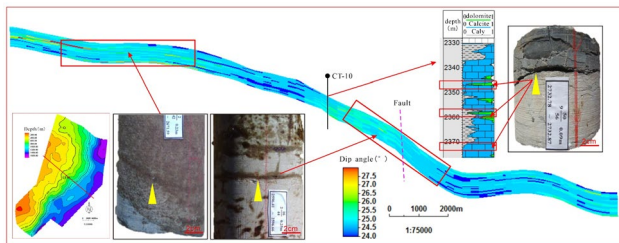
Fig. 23 Distributions of different genetic low-angle shear fractures in KT-I formation of the NT oilfield

the formation pressure coefficient in the study area is 2.43. The simulation results once again confirm that the study area has developed a strong abnormally high pressure.

Discussion

Although there are some differences among type I low-angle shear fractures, type II low-angle shear fractures and type III low-angle shear fractures, they all belong to shear fractures, and the formation mechanism of fractures dip angle can be analyzed according to the stress simulation results and Coulomb–Moore rupture criterion (Fossen 2016; Liu 2015). The formula for calculating the dip angle of shear fractures based on the Coulomb–Moore fracture criterion is (Ju and Sun 2016):

$$\theta = 45° + \frac{\varphi}{2} \tag{26}$$

where θ is the angle between the minimum principal stress and the fracture surface, and it is also the angle between the normal direction of the fracture surface and the maximum principal stress. The angle between the maximum principal stress and the fracture surface is $90 - \theta$. φ is the internal friction angle of the rock. The calculation results display that the dip angle of shear fractures is between 24° and 29° (Fig. 22a and b). The fractures with a dip angle of 24°–29° are the type II low-angle shear fractures identified in this paper. The previous studies on rock rupture show that the shear fracture in rock is generally about 30° with the maximum principal stress, thus the calculation result of the fracture dip angle in this paper is within a reasonable range. In addition, the stress simulation results explain the geological phenomenon that the fractures with a dip angle of 20°–30° are very developed in cores.

The included angle between the strata near the faults in the study area and the horizontal plane is about 20°, and the included angle between the LAFs and the horizontal plane is 24°–29°, thus the LAFs formed in this area are nearly parallel to the beddings, which is the type I low-angle shear fractures identified in this study (Fig. 23). Due to the influence of the tectonic inversion, the type I low-angle shear fractures are mainly nearly horizontal LAFs at present. This phenomenon reflects the influence of stratum dip angle on the occurrence of low-angle fractures.

In addition to the type I and type II low-angle shear fractures analyzed above, a large number of type III low-angle shear fractures related to the beddings are also developed in the study area. Type III low-angle shear fractures develop along sedimentary bedding or foliation, which is influenced by the pre-existing weak fabrics of the rock; hence, the rock rupture mechanism follows the non-coordination criterion. Because of the weak fabrics, the cohesion and internal friction angle of the rock will be reduced, causing the compressive strength of the rock will be significantly reduced, that is, the rupture envelope in Fig. 15 is smaller than that of the intact rock, and the fractures are easier to develop.
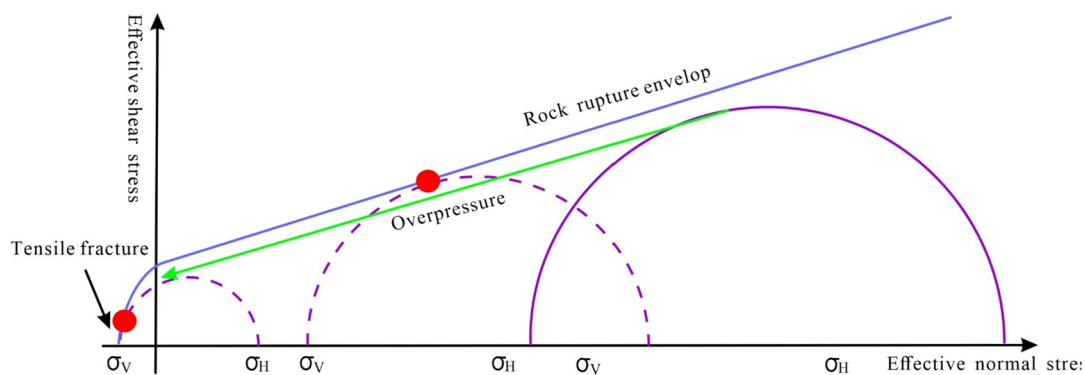
Fig. 24 Formation mechanism of tensile fractures

Therefore, a large number of type III low-angle shear fractures are developed in the study area.

When the second period of the LAFs in the study area was formed, the study area was in a state of intense horizontal compression, and the vertical direction was the minimum principal stress direction. Therefore, in the absence of other factors, the minimum principal stress in the study area should be compressive stress, and all fractures should be shear fractures. However, the study area develops many tensile fractures. The previous studies have pointed out that abnormally high pressure can change the fracture type from shear fracture to tensile fracture (Fig. 24) (Hillis 2003; Kang and An 2016; Luo et al. 2015). During the formation of the LAFs in the NT oilfield, intense abnormally high pressure developed, and the results of in situ stress field simulation also confirmed that the abnormally high pressure resulted in the development of tensile fractures in the study area. The influence mechanism of abnormally high pressure on fracture types is as follows: Due to the increase in fluid pressure, both the maximum principal stress and the minimum principal stress decrease, and the difference between the maximum principal stress and the minimum principal stress also decreases. Therefore, with the increase in pore pressure, the Mohr circle keeps moving in the negative direction of

the coordinate axis, and the radius of the Mohr circle keeps decreasing. Finally, due to the influence of pore pressure, the minimum principal stress changes from positive value to negative value, that is, the stress gradually changes from extrusion state to tension state. It should be noted that the abnormally high pressure is not only the direct cause of the formation of tensile fractures, but also promotes the development of shear fractures.

Due to the influence of fault on the disturbance of the stress field, the zone near the fault develops not only the shear fractures parallel to the fault and shear fractures conjugated with the fault, but also tensile fractures nearly perpendicular to the fault (Sun et al. 2017a, b). This phenomenon is mainly because the hanging wall and footwall of the fault drag each other during the thrust fault activity, thus the tension fractures are formed in the horizontal direction perpendicular to the reverse fault plane. The simulation results of the in situ stress field in the NT oilfield show that the displacement of the hanging wall and footwall of the fault in the study area is between 0 and 0.27 m. Due to the mutual drag between the hanging wall and the footwall of the fault, there are conditions for the development of tension fractures (Fig. 25).
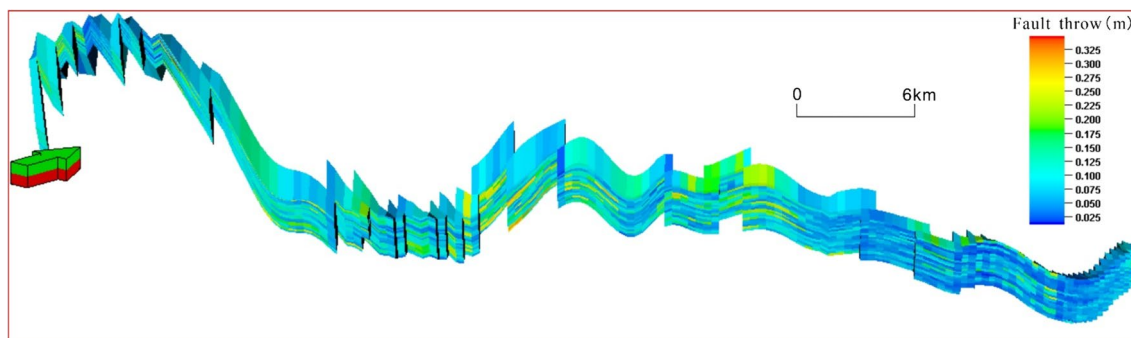

Fig. 25 Fault throw distribution of KT-I formation in the NT oilfield

Conclusions

1. The low-angle fractures (LAFs) in the NT oilfield are mainly shear fractures, with a percentage of the number of 90.2%, while the percentage of the number of tensile fractures is only 9.8%. According to the dip angle of LAFs and the beddings in the rocks, the low-angle shear fractures in the study area can be further divided into three types, including near-horizontal LAFs in the non-weak fabrics section (type I low-angle shear fractures), the LAFs having a certain angle with bedding in the non-weak fabrics section (type II low-angle shear fractures) and near-horizontal LAFs in the weak fabrics section (type III low-angle shear fractures).

2. The mechanical genetic mechanism of LAFs caused by fault propagation folds under the compression background was revealed in this paper by restoring the paleostructure and simulating the crustal stress field. The LAFs are formed under the joint influence of tectonic movement and abnormally high pore pressure. The burial depth of the strata is moderate, with the development of Anderson stress type II, which means the development of compression tectonic background. Under the compression background, the fault propagation folds develop (knee-fold structure is a typical fault propagation fold), which is the mechanical basis for the formation of low-angle shear fractures. The overlying salt rock strata is an excellent cap rock, leading to the development of fluid overpressure. The abnormally high pressure of the fluid not only promotes the formation of low-angle shear fractures, but also induces the development of low-angle tensile fractures.

3. The formation mechanical mechanism of different types of LAFs is different. The formation of type I and type II low-angle shear fractures follows the Coulomb–Moore criterion, but type I low-angle shear fractures are formed in strata with a certain dip angle, while type II low-angle shear fractures are formed in nearly horizontal strata. Type III low-angle shear fracture is formed under the comprehensive influence of pre-existing weak fabrics and strong horizontal extrusion, and follows the non-coordination criterion. Low-angle tensile fractures are mainly formed under the influence of fluid abnormally high pressure and thrust fault in the study area, and they follow the Griffith criterion.

Declarations

References

Bagrintseva KI (2015) Carbonate reservoir rocks. Wiley, Hoboken, pp 1–10

Brunet M, Volozh YA, Antipov MP, Lobkovsky LI (1999) The geodynamic evolution of the Precaspian basin (Kazakhstan) along a north–south section. Tectonophysics 313:85–106

Burra A, Esterle JS, Golding SD (2014) Horizontal stress anisotropy and effective stress as regulator of coal seam gas zonation in the Sydney Basin, Australia. Int J Coal Geol 132:103–116

Du X, Jiao X, Zheng H (1995) Abnormal pressure and hydrocarbon accumulation. Earth Sci Front 2(3):137–147

Du G, Cang H, Zhang S, Cao Q (2016) Development pattern and genesis of fractures in block L of Khorat Basin. Spec Oil Gas Reserv 23(6):21–25

Fossen H (2016) Structural geology. Cambridge University Press, London, pp 1–77

Hillis RR (2003) Pore pressure/stress coupling and its implications for rock failure. Geol Soc Lond Spec Publ 216:359–368

Hu Y, Xia B, Wang Y, Wan Z, Cai Z (2014) Tectonic evolution and hydrocarbon accumulation model in eastern Precaspian Basin. Sediment Geol Tethyan Geol 34(3):78–81

Huang W, Xu F, Liu C (2022) Seismic prediction of fractures and vugs in deep-water sub-salt lacustrine carbonates: taking F oilfield in Santos Basin, Brazil as an example. Oil Gas Geol 43(2):445–455

Jika HT, Onuoha MK, Okeugo CG, Eze MO (2020) Application of sequential indicator simulation, sequential Gaussian simulation and flow zone indicator in reservoir-E modelling; Hatch Field Niger Delta Basin, Nigeria. Arab J Geosci 13:1–19

Jing Z, Li G, Zhang Y, Wang R, Xie T, Cui J, Liu W, Dai H (2021) Salt structure characteristics and deformation mechanism in the

eastern margin of Precaspian basin: the implication of physical simulation. Acta Geol Sin 95(05):1459–1468

Jiu K, Ding WL, Li CY, Zeng WT (2012) Advances of paleostructure restoration methods for petroliferous basin. Lithol Reserv 24(1):13–19

Ju W, Sun W (2016) Tectonic fractures in the Lower Cretaceous Xiagou Formation of Qingxi Oilfield, Jiuxi Basin, NW China. Part two: numerical simulation of tectonic stress field and prediction of tectonic fractures. J Pet Sci Eng 146:626–636

Kabiyev Y, Carpenter D, Johns M, Collins J (2012) Fracture characteristics of a carbonate platform, Kashagan field, Kazakhstan. In: 2nd EAGE international conference

Kang D, An S (2016) Pore pressure/stress coupling progress and its specificity in shale-oil reservoir. Chin J Eng Geophys 13(04):538–545

Li C, Zhao L, Liu B, Liu H, Li J, Fan Z, Wang J, Li W, Zhao W, Sun M (2021) Origin, distribution and implications on production of bedding-parallel fractures: a case study from the Carboniferous KT-I formation in the NT Oilfield, Precaspian Basin Kazakhstan. J Pet Sci Eng 196:107655

Liu Z (2010) The finite element simulation of fracture in buried hills of Jizhong region. Thesis, China University of Petroleum (Huadong)

Liu S (2015) Study on prediction of carbonate fractures based on multi-scale. Thesis, China University of Petroleum (Huadong)

Luo Y, Zhao Y, Chen H, Su H (2015) Fracture characteristics under the coupling effect of tectonic stress and fluid pressure: a case study of the fractured shale oil reservoir in Liutun subsag, Dongpu Sag, Bohai Bay Basin Eastern China. Pet Explor Dev 42(2):196–205

Ma Y, Cai X, Yun Lu, Li Z, Li H, Deng S, Zhao P (2022) Practice and theoretical and technical progress in exploration and development of Shunbei ultra-deep carbonate oil and gas field, Tarim Basin, NW China. Pet Explor Dev 49(1):20

Manchuk JG, Deutsch CV (2012) Implementation aspects of sequential Gaussian simulation on irregular points. Comput Geosci 16:625–637

Miao Q, Wang Y, Zhu X, Yu B, Jiang J (2013) Sequence stratigraphy of Carboniferous in Eastern Margin of PreCaspian Basin. Xinjiang Pet Geol 34(04):483–487

Mo W, Zheng Y, Zhang W, Guan P (2007) Analysis of the youquanzi oil-bearing structure in Qaidam basin. Oil Gas Geol 28:324–328

Nelson R (2001) Geologic analysis of naturally fractured reservoirs. Elsevier, New York, pp 1–330

Ostadhassan M, Zeng Z, Zamiran S (2012) Geomechanical modeling of an anisotropic formation-Bakken case study. In: 46th US rock mechanics/geomechanics symposium

Qiu S (2017) Establishment and application of three pressure profile in deep gas reservoir of shuangyushi structure. Thesis, Southwest Petroleum University

Schmid K (2018) A geomechanical property model of the Trattnach Oil Field in the Upper Austrian Molasse basin. Thesis, University of Leoben

Séjourné S, Malo M, Savard MM, Kirkwood D (2005) Multiple origin and regional significance of bedding parallel veins in a fold and thrust belt: the example of a carbonate slice along the Appalachian structural front. Tectonophysics 407:189–209

Sima L, Li Q, Yang Y, Zhang F (2014) Effectiveness evaluation of fractured carbonate reservoir with high porosity and low permeability: a case from c group of X Oilfield in the Middle East. Sci Technol Eng 14(27):1671–1815

Smart KJ, Ferrill DA, Morris AP (2009) Impact of interlayer slip on fracture prediction from geomechanical models of fault-related folds. AAPG Bull 93:1447–1458

Smart KJ, Ferrill DA, Morris AP, Bichon BJ, Riha DS, Huyse L (2010) Geomechanical modeling of an extensional fault-propagation fold: big brushy canyon monocline, Sierra Del Carmen, Texas. AAPG Bull 94:221–240

Sun L, Kang Y, Wang J, Jiang S, Zhang B, Gu J, Ye J, Zhang S (2017a) Vertical transformation of in situ stress types and its control on coalbed reservoir permeability. Geol J China Univ 23(1):148–156

Sun S, Hou G, Zheng C (2017b) Fracture zones constrained by neutral surfaces in a fault-related fold: insights from the Kelasu tectonic zone, Kuqa Depression. J Struct Geol 104:112–124

Tavener E, Flottmann T, Brooke-Barnett S (2017) In situ stress distribution and mechanical stratigraphy in the Bowen and Surat basins, Queensland, Australia. Geol Soc Lond Spec Publ 458:31–47

Thiercelin MJ, Plumb RA (1994) Core-based prediction of lithologic stress contrasts in east Texas formations. SPE Form Eval 9:251–258

Tian N, Yan S, Hui G (2015) Controlling factors of petroleum accumulation in pre-salt strata in south uplift of Pre-Caspian Basin. Xinjiang Pet Geol 36(1):116–120

Tong HM, Cai DS, Wu YP, Li XG, Li XS, Meng L (2011) Activity criterion of pre-existing fabrics in non-homogeneous deformation domain. Sci China Earth Sci 41(2):158–168

Wang S (2012) Genesis and characterization techniques of carbonate reservoir under overpressure. Thesis, China University of Geoscience (Beijing)

Wang X, Sun Y, Pang Y (2000) Distribution of the fractures and ground stress in fuyang reservoir of sanzhao area and its effect on water flooding development. Pet Geol Oil Dev Daqing 2000(05):9–12

Wang Y, Zhang Z, Zhang B, Yun J, Liu S, Song H (2014) Discovery of large kink-band structures and petroleum exploration implications in Bachu area, Tarim Basin. Oil Gas Geol 35(6):914–924

Zeng L, Qi J, Wang Y (2007) Origin type of tectonic fractures and geological conditions in low-permeability reservoirs. Acta Pet Sin 28(4):52

Zhang B, Li S, Zhang J, Zheng Y, Zhang Z (2010) Kink, kink-band and conjugate kink-band: a probably potential new type of structural trap. Nat Gas Ind 30(2):32–39

Zheng Y, Mo W (2007) A new idea for petroleum exploration in Qaidam basin. Pet Explor Dev 34(1):13–18

Zhu S, Li J, Chen H, Hu Y, Yang F, Xu X (2018) Hydrocarbon accumulation condition and main controlling factors of sub-salt strata in southern uplift of pre-Caspian basin. Pet Geol Eng 32(03):28–32